Thesis for The Degree of Doctor of Philosophy

Local lattice distortions in refractory high-entropy alloys

Yao Hu

Department of Physics
Chalmers University of Technology
Gothenburg, Sweden, 2025

Local lattice distortions in refractory high-entropy alloys

Yao Hu

ISBN 978-91-8103-353-3

Acknowledgements, dedications, and similar personal statements in this thesis, reflect the author's own views.

Doktorsavhandlingar vid Chalmers tekniska högskola
Ny serie nr 5810
ISSN 0346-718X
https://doi.org/10.63959/chalmers.dt/5810

Department of Physics
Chalmers University of Technology
SE-412 96 Gothenburg
Sweden
Telephone: +46 (0)31-772 1000

Cover:
The neutron/X-ray beams come from the left and interact with a bcc-structured unit cell, where different colours represent different metallic atoms. These atoms are displaced from their ideal positions due to size mismatch and are simultaneously undergoing thermal vibrations. On the right is an illustration of the resulting scattering data: the upper panel depicts the diffraction pattern, and the lower panel depicts the pair distribution function.

Printed by Chalmers Digitaltryck
Gothenburg, Sweden 2025

Local lattice distortions in refractory high-entropy alloys

Yao Hu

Department of Physics
Chalmers University of Technology

Abstract

Refractory high-entropy alloys (RHEAs) are a novel class of alloys known for their exceptional mechanical properties at high temperatures, making them promising candidates for next-generation aerospace applications. RHEAs typically composed of multiple principal elements in (near-)equiatomic concentrations. A key factor contributing to their strength is local lattice distortion (LLD), which arises from atomic size mismatch, charge transfer effects and force constant variations among constituent elements. LLDs have been shown to contribute to solid solution strengthening and phase stabilisation, making them vital for mechanical performance and reliable processing of RHEAs. However, LLD remains poorly understood, particularly regarding quantification due to experimental challenges.

Neutron and synchrotron X-ray total scattering are the primary techniques used in this thesis, which enables simultaneous probing of both long-range order and local disorder. Quantitative determination of LLDs was done through small-box modelling of the pair distribution functions in real space, and through Rietveld refinement of diffraction patterns in reciprocal space. Molecular dynamics (MD) simulations provide the vibrational density of states (VDOS), allowing separation of scattering from dynamic (or thermal) and static atomic displacements. Specific heat measurements analysed using Debye approximation offer an alternative route for estimating thermal contributions.

It is shown that LLDs in bcc-structured RHEAs can be accurately quantified using both reciprocal- and real-space methods. A comprehensive methodology, combining variable-temperature neutron total scattering experiments with VDOS from MD simulations, revealed a negative temperature dependence of LLDs in a HfNbTaTiZr RHEA, which was further confirmed and extended to NbTaTiZr and MoNbTaW. Additional studies on alternative quantification methods and the effect of chemical heterogeneity establish a framework for understanding LLDs in RHEAs.

Keywords

local lattice distortion, refractory high-entropy alloys, atomic displacements, thermal vibration, neutron scattering, synchrotron X-ray diffraction, total scattering, pair distribution function

List of Publications

Appended papers

This thesis is based on the work contained in the following papers, referred to by Roman numerals in the text:

I **Quantifying local lattice distortions in refractory high-entropy alloys**
Yao Hu, Lewis R. Owen, Helen Y. Playford, Aina Edgren, Sheng Guo, Magnus Hörnqvist Colliander
Physical Review Materials **8**, 083602 (2024)

II **Effect of chemical segregation on accuracy of local lattice distortions determination by pair distribution functions**
Yao Hu, Sheng Guo, Magnus Hörnqvist Colliander
AIP Advances **14**, 115310 (2024)

III **Temperature dependence of local lattice distortions in the refractory high-entropy alloy HfNbTaTiZr**
Yao Hu, Paul Erhart, Lewis R. Owen, Gabriel E. Pérez, Helen Y. Playford, František Lukáč, Severin Jakob, Mattias Thuvander, Janez Dolinšek, Sheng Guo, Magnus Hörnqvist Colliander
In manuscript

IV **Effect of composition on the temperature dependence of local lattice distortions in refractory medium-entropy alloys**
Yao Hu, Gabriel J. Cuello, Henry E. Fischer, Janez Dolinšek, Jiatu Liu, Lewis R. Owen, Sheng Guo, Magnus Hörnqvist Colliander
In manuscript

Disclaimer: Parts of this thesis are based on my licentiate thesis entitled *Quantification of local lattice distortions in refractory high-entropy alloys by scattering-based techniques* (Chalmers University of Technology, 2024).

My contributions to the appended papers

I I performed the high-resolution diffraction experiments with assistance from beamline scientists and colleagues. I analysed the total scattering and diffraction data. I was involved in the SEM experiments. I wrote the first draft of the manuscript and contributed to its reviewing and editing.

II I did the simulation study with guidance from my supervisor. I wrote the first draft of the manuscript and contributed to its reviewing and editing.

III I performed the neutron total scattering experiments with assistance from beamline scientist and colleagues, processed and analysed the data. I analysed the vibrational density of states and specific heat data. I wrote the first draft of the manuscript and contributed to its reviewing and editing.

IV I performed the neutron total scattering and synchrotron X-ray diffraction experiments with assistance from beamline scientists and colleagues, processed and analysed the data. I analysed the specific heat data. I wrote the first draft of the manuscript and contributed to its reviewing and editing.

Other publications

The following publications were published during my PhD studies, or are currently in submission/under revision. However, they are not appended to this thesis, due to contents overlapping that of appended publications or contents not related to the thesis.

I **Anisotropic secondary phases in $Mo(Si,Al)_2$ ceramics investigated by neutron diffraction**
Kristine Bakken, Aina Edgren, Yao Hu, Ivan da Silva, Erik Ström, Magnus Hörnqvist Colliander
Materials Letters **406**, 139927 (2026)

To my dear motherland.

Preface

This thesis is the result of my PhD research conducted under the supervision of Prof. Magnus Hörnqvist Colliander and Prof. Sheng Guo, at Microstructure Physics Division, Department of Physics, Chalmers University of Technology, during the period 2022-2026.

The PhD project is a part of the Swedish National Graduate School in Neutron Scattering (SwedNess), financially supported by the Swedish Foundation for Strategic Research (Stiftelsen för Strategisk Forskning, SSF) with grant ID GSn15-0008. The program aims to educate the next generation of neutron facility users in order to strengthen the Swedish competence in anticipation of the European Spallation Source (ESS) coming online.

The thesis starts with an introduction (Chapter 1) to the studied object—local lattice distortions in high-entropy alloys, the motivation and the scope of the thesis. This is followed by dedicated chapters giving more detail on high-entropy alloys (Chapter 2) and local lattice distortions (Chapter 3), respectively, where I explain some fundamental concepts and the relevant background. I next explain the methodology of the determination of local lattice distortion (Chapter 4), how the related experiments are performed, and the data is analysed (Chapter 5). I finish with a summary of the main results (Chapter 6).

During my PhD study, I have taken several courses (64.5 ECTS) covering topics such as neutron and X-ray scattering, data analysis and statistics, materials science, generic courses on teaching and academic writing etc. I also attended hands-on training in neutron scattering at TU Delft, the Netherlands (neutron diffraction and neutron imaging), and at PSI, Switzerland (neutron reflectometry and inelastic neutron scattering). In addition, I received theoretical and practical training in synchrotron radiation techniques through the MATRAC school at P02.1 beamline (powder X-ray diffraction) at DESY, Germany, and at DanMAX (high-pressure powder X-ray diffraction) and NanoMAX (nano-focused X-ray imaging) beamlines at MAX IV, Sweden. I took a two-month extended stay: one month at the Polaris beamline at ISIS Neutron and Muon Source in the UK, hosted by Dr. Helen Playford, and one month with Dr. Lewis Owen's group at University of Sheffield. As part of the SwedNess program, I also participated in a one-week scientific visit to J-PARC in Japan. During my PhD, I have been granted four beamtimes through proposal applications, two at a synchrotron facility (P21.1 at DESY,

Germany) and two at neutron facilities (GEM at ISIS, UK, and D4 at ILL, France). In addition, I have participated in five other synchrotron and one neutron beamtime experiments across Europe. Regarding scientific communications, I have participated in eight national and international conferences and delivered four oral presentations (EUROMAT, MSE, Swedish Neutron Week).

Acknowledgment

I always feel that acknowledgment is something you rehearse a hundred times in your mind, yet finally write in a rush—often with the deadline ticking loudly (I confess as I write this it's just hours before printing). It feels a bit like trying to say something really important at the very moment the person on the other end has already hung up.

The truth is that I cannot find the words to express my thankfulness to the people who have looked after me over the years. There are so many of them. And I have never been the kind of person who is good with words. More than once I have wished I had told someone, at the right moment, how much what they did truly meant to me. So, I hope these few lines can at least carry a fraction of the gratitude I feel, and convey what I have often failed to say in person.

Four years is a short time—at least it feels that way. I can still clearly remember arriving here, my first time abroad, just as the pandemic was finally easing. I remember my first fika with my colleagues, and how new and unfamiliar everything felt. It all went by so quickly that before I realised it, I was already here.

As their only child, my parents have never stopped me from pursuing my dreams. They never once hesitated and unconditionally supported me to continue my study in Sweden, even though it means that I have to be over 7000 kilometres away from them. In this sense, four years is a long time.

Now I find myself lost for words, so perhaps it is best to stop here.

Contents

Chapter 1

Introduction

1.1 Advances in metallic materials

The development and application of metallic materials have played a critical role throughout human history. Over the past centuries, the invention and utilisation of new metallic materials have substantially driven societal and technological progress. Traditionally, alloys are composed of one or two primary metallic elements with a minor addition of other metallic or non-metallic elements to achieve desired properties such as high strength and hardness, and corrosion resistance. One of the best examples is iron—this single element can be used in alloys for such a wide range of applications—cookware, engine blocks, railway tracks and more, simply by adjusting the carbon content slightly (0.05–2%), and this does not include the extensive families of other metal-based alloys with thousands of different compositions and diverse properties. And yet, this is not the endpoint.

In 2004, a new alloy design concept was proposed by Yeh [1] and Cantor [2], introducing the concept of high-entropy alloys (HEAs). This innovative class of materials, comprised of five or more elements in nearly equiatomic concentrations (hence also referred to as multi-principal element alloys, MPEAs), was found to form a simple solid solution phases rather than complex intermetallic compounds due to their high configurational entropy. The unique compositional space inherent in HEAs opens up more potential for the design of metallic materials with superior mechanical properties (see Figure 1.1) and has promising applications [3], [4].

1.2 Gaps and challenges

The pursuit of high-performance structural materials targeting applications under extreme conditions has driven the advancement of refractory HEAs (RHEAs), which are considered promising candidates for next-generation aerospace applications [5]. Despite the excellent properties of existing nickel-based superalloys, their operational temperature is typically limited to below

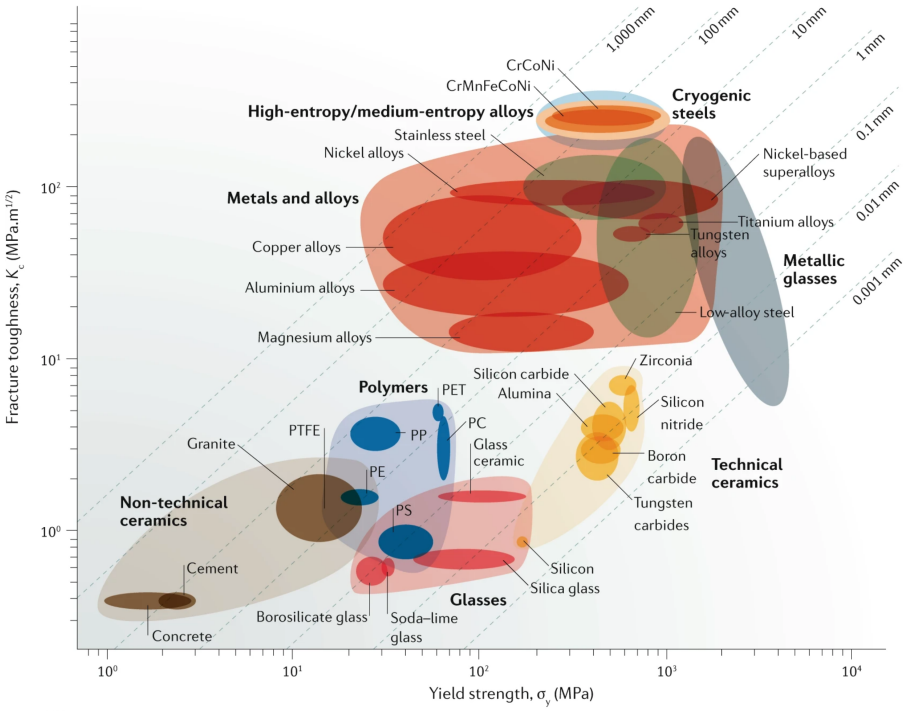

Figure 1.1: Ashby plot of fracture toughness versus yield strength showing the remarkable mechanical properties of representative HEAs among other materials [3]. *Reproduced with permission from Springer Nature.*

1150°C without auxiliary cooling, thereby constraining engine efficiency. Therefore, RHEAs are being actively studied as potential replacements for conventional high-temperature materials. Recent studies have proposed that one of the origins of the excellent mechanical properties of RHEAs is the presence of local lattice distortions (LLDs) [6], [7], [8], [9]. LLD refers to the static displacement of atoms away from their ideal lattice sites because of variations in atomic radius and electronegativity among the constituent elements and differences in force constants. However, the definition and quantification of LLD still remains a subject of debate. The inconsistencies primarily come from the experimental challenge of accurately measuring such subtle structural features at the atomic scale. Moreover, LLDs are intrinsically coupled with atomic thermal vibrations, making it difficult to unambiguously separate these two contributions. So far, attempts to measure LLDs have only been made at room temperature and at cryogenic temperatures, with the assumption that they are temperature-independent. In addition, the effect of temperature on LLDs remains a mystery, but it is still an important issue, especially for RHEAs which are intended for high-temperature applications. Systematic analysis and comprehensive understanding of LLD are essential for enabling targeted design strategies for future high-performance engineering materials.

1.3 Scope of the thesis

The thesis focus on understanding the LLDs in body-centred cubic (bcc) structured RHEAs, both qualitatively and quantitatively. The primary techniques used is neutron total scattering, owing to its sensitivity to atomic-scale disorder and its independence from atomic form factor, which is essential in determining the atomic displacements. Complementary techniques of specific heat measurements and molecular dynamics (MD) simulations were employed to characterise thermal vibrations of atoms and to investigate the temperature dependence of LLDs. Several bcc RHEAs were systematically studied to identify the elemental origins of LLDs. In addition, alternative approaches for estimating the thermal component such as Debye approximation, and the effect of chemical heterogeneity were examined, in order to broaden the scope of the study. The following research questions are posed as guiding objectives and will be answered at the end of this thesis:

- How can the thermal displacements be accurately separated from the total atomic displacements, and are LLDs truly substantial in bcc-structured RHEAs?
- How does chemical segregation in dendritic microstructures impact the accuracy of LLD determination?
- Does the magnitude of LLDs vary with temperature, and is this temperature dependence a generic feature of bcc-structured RHEAs?
- What are the elemental origins of LLDs?

Chapter 2

High-entropy alloys

2.1 Introduction

The term high-entropy alloy (HEA), usually refers to the group of alloys containing multiple principal elements in equiatomic or near-equiatomic proportions (typically 5–35 % for each element for an alloy that contains at least five elements [1]). The term "high-entropy" refers to the increased configurational entropy that comes from mixing several elements, which is defined as:

$$\Delta S_{\text{mix}} = -R \sum_{i}^{n} x_i \ln x_i \tag{2.1}$$

where R is the gas constant and x_i is the concentration of element i. A general definition considers alloys with $\Delta S_{\text{mix}} \geq 1.5R$ as HEAs, which excludes a small number of alloys allowed by the standard definition [10]. However, alloys with complex compositions do not necessarily have high configurational entropy. The entropy of an alloy changes with temperature and reaches its maximum at high temperatures, whereas HEAs, which are processed and used at relatively low temperatures, can have local chemical order and complex enthalpic interactions [4], [11]. These issues demonstrate the challenges in the use of the entropy definition. There are some other terms that avoid using the magnitude of entropy and include multi-principal element alloys (MPEAs) or compositionally complex alloys/complex concentrated alloys (CCAs). To broaden the study of LLDs, two quaternary alloys that may not strictly fit the HEA definition are also included. For simplicity, the term HEA is adopted throughout this thesis, with the understanding that the thermodynamic definition of entropy may not be fully satisfied.

Over the past twenty years, several characteristics of HEAs have been identified. Among these, four "core effects" stand out: high entropy, lattice distortion, sluggish diffusion and cocktail effects [12]. These were initially proposed based on early research findings and have since been discussed and evaluated against a more extensive range of published data [4]. Among these "core effects", lattice distortion is considered one of the most fundamental and

Table 2.1: Entropy of equiatomic alloys (ΔS_{mix}) with respect to the type of elements (n). R is the gas constant.

n	1	2	3	4	5
ΔS_{mix}	0	$0.69R$	$1.10R$	$1.39R$	$1.61R$

important factors contributing to the remarkable properties of HEAs [6], [13], [14], and it is therefore the primary focus of this thesis. It will be discussed in more detail in Chapter 3.

One of the essential features of HEAs, high entropy, contributes to lowering the Gibbs energy and helps to stabilise solid solutions against the formation of intermetallic compounds. The Gibbs free energy of a mixing system is defined as:

$$\Delta G_{\text{mix}} = \Delta H_{\text{mix}} - T\Delta S_{\text{mix}} \tag{2.2}$$

where ΔG_{mix} and ΔH_{mix} are the Gibbs free energy and enthalpy, respectively. The values of mixing entropy ΔS_{mix} of equiatomic HEAs (with maximised entropy in the system), calculated using Equation (2.1), are presented in Table 2.1. High mixing entropy typically suggests a reduced probability for ordering and segregation, but this does not apply to compounds with significantly large (negative) heats of formation, such as Al-Ti, Al-Hf and Al-Zr intermetallics. Consequently, one can infer that if the magnitude of the entropy could be so pronounced (especially at high T) that it compensates for the enthalpy of the formation of intermetallic compounds, the system would have the opportunity to form solid solutions to reach the lowest Gibbs energy for stability, as schematically illustrated in Figure 2.1.

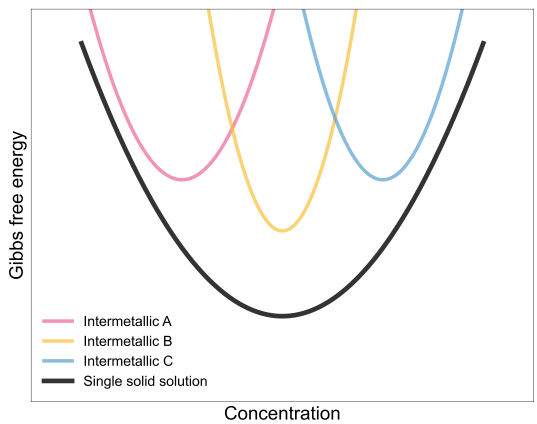

Figure 2.1: Schematic illustrations of the single solid solution feature of HEAs, resulting from the reduction in Gibbs free energy [3].

2.2 Refractory high-entropy alloys

Various crystal structures, such as face-centred cubic (fcc), body-centred cubic (bcc), and hexagonal close-packed (hcp), have been widely reported in HEAs. Among these, one of the first and most studied examples is the fcc-structured CoCrFeMnNi (commonly known as the Cantor alloy [2]), along with alloys based on the 3*d*-transition metals (Ti, V, Cr, Mn, Fe, Co, Ni, Cu). HEAs composed of these elements, however, have not shown high-temperature properties that could significantly exceed those of conventional Ni-based superalloys.

Refractory high-entropy alloys (RHEAs) were first proposed by Senkov et al. in 2010 [17] with the aim of making new high-temperature structural materials using the HEA design strategy. The early RHEAs were typically composed of refractory elements such as Mo, Nb, Ta, V, W. As shown in Figure 2.2A, the incorporation of these elements significantly enhances yield strength at elevated temperatures (above 1000 °C), where the strength of superalloys decreases rapidly. Although RHEAs such as MoNbTaW and MoNbTaVW show exceptional high-temperature strength, their applications are limited due to poor ductility at room temperature since most bcc (and/or B2) structured RHEAs show a ductile-to-brittle transition above room temperature [18]. It is reported that adding elements from group IV, such as Ti, Zr, and Hf, typically enhances the ductility of alloys [19]. Evidence from first-principles calculations suggests that alloying group IV and V elements can transform group VI metals (Mo, W) from intrinsically brittle to intrinsically ductile [20]. Benefiting from this effect, HfNbTaTiZr [21], [22] and its derivatives (such as HfNbTiZr [23] and HfTaTiZr [24]) exhibit significantly improved ductility compared to MoNbTaW and MoNbTaVW, as can be seen in Figure 2.2B. Their exceptional ductility makes processing easier, and places them among the most extensively studied RHEAs, possessing a balance between strength and ductility.

The inclusion of group IV elements seems to increase the magnitude of LLDs. Tong et al. [26] observed that RHEAs containing Zr and/or Hf have

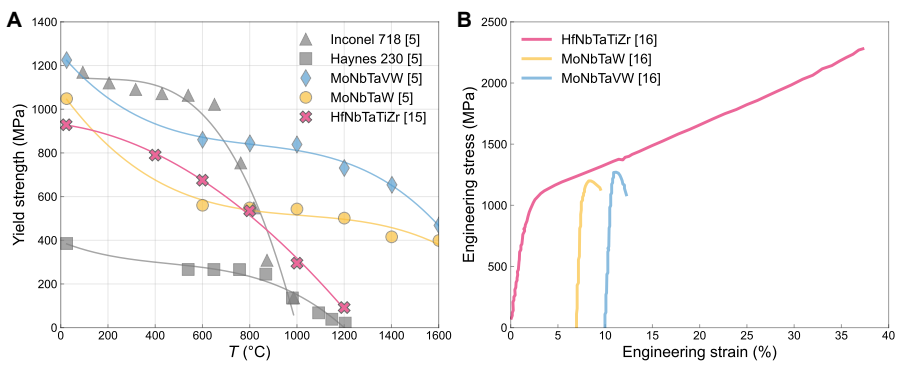

Figure 2.2: (**A**) Comparison of variable-temperature yield strength, showing enhanced strength of RHEAs compared to superalloys at high temperatures [5], [15]. (**B**) Significantly improved ductility of HfNbTaTiZr in comparison with the other two RHEAs. *Reprinted from Ref. [16] with permission from Elsevier.*

Table 2.2: Melting point of some common elements presented in RHEAs.

Element	Ti	Zr	Hf	V	Nb	Ta	Mo	W
Melting point† (K)	1933	2125	2500	2163	2741	3269	2883	3683

† From [25].

pronounced LLDs, primarily due to the significant atomic size and Fermi level differences between Zr/Hf atoms and the atoms of the other constituent elements. This was one of the key motivations for selecting this alloy as the primary study subject in this thesis.

It should be noted that differences in the melting points of the constituent elements (listed in Table 2.2) often leads to chemical segregation. As a result, dendritic microstructures are frequently observed in RHEAs [5], [26], [27], [28], as shown in Figure 2.3. Such segregation can affect the quantification of LLDs, which will be further discussed in Chapter 6.

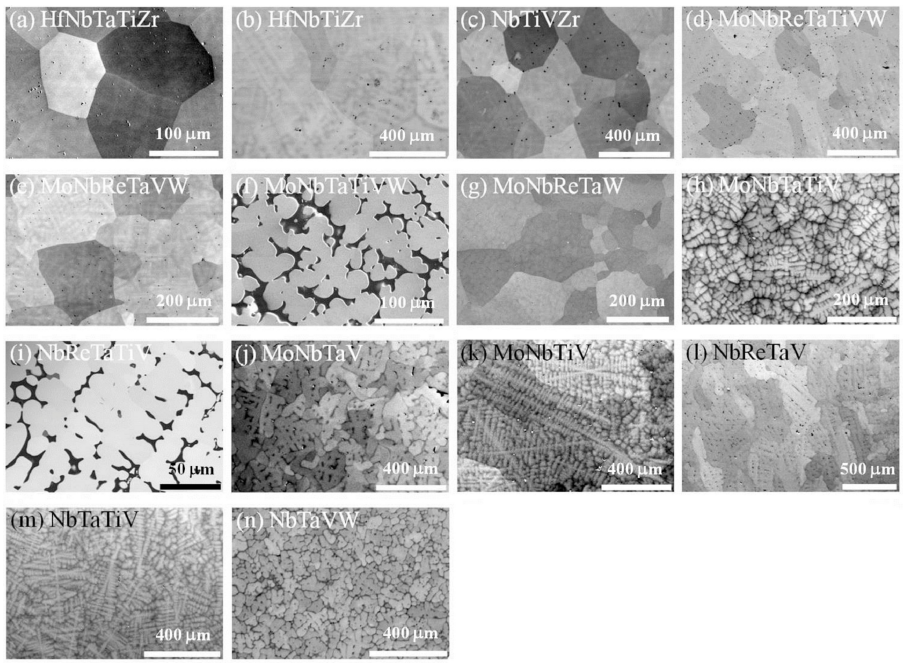

Figure 2.3: Typical dendritic microstructures of some RHEAs. *Reprinted from Ref. [26] with permission from Elsevier.*

Chapter 3

Local lattice distortions

3.1 Definitions of LLDs

One of the key challenges in the study of LLDs is the absence of a universally accepted definition. Various publications define LLDs differently, making it difficult to compare results across different materials systems. In this section, both qualitative and quantitative definitions of LLDs in the form of local lattice strains are discussed.

3.1.1 Lattice strain

A straightforward way of viewing LLDs is treating them as a type of strain, specifically, local lattice strain. Though the term "strain" is commonly used in metallurgical contexts, one should clarify that the lattice strain is distinct from other types of strains. According to the classification by Owen and Jones [29], strain is categorised into three types: macrostrain, microstrain and lattice strain, each with its unique characteristics and effects on HEAs. The differences among these strains can be schematically illustrated using a 2D lattice, as shown in Figure 3.1. Macrostrain (Figure 3.1B) refers to large-scale or bulk deformations across the entire structure, typically resulting in global changes in the alloy's shape or volume (such as stretching, compression, or bending) and leads to variations in the overall inter-planar spacing. Microstrain (Figure 3.1C) refers to small-scale deformation around specific areas like defects, dislocations, or grain boundaries, which cause slight variations in the inter-planar spacing within the crystal structure. The lattice strain (Figure 3.1D) is the static displacements of atoms from their ideal lattice sites, in order to accommodate the size differences among atoms.

It should be noted that despite the presence of LLDs, the overall crystal structure of HEAs remains intact, as the average bond length aligns with the lattice parameter which should also remain unchanged. Although individual atoms may deviate from their ideal positions, these distortions are not significant enough to transform the crystalline structure into an amorphous form, thus preserving the crystallinity of HEA [29]. Such variations in the local structure

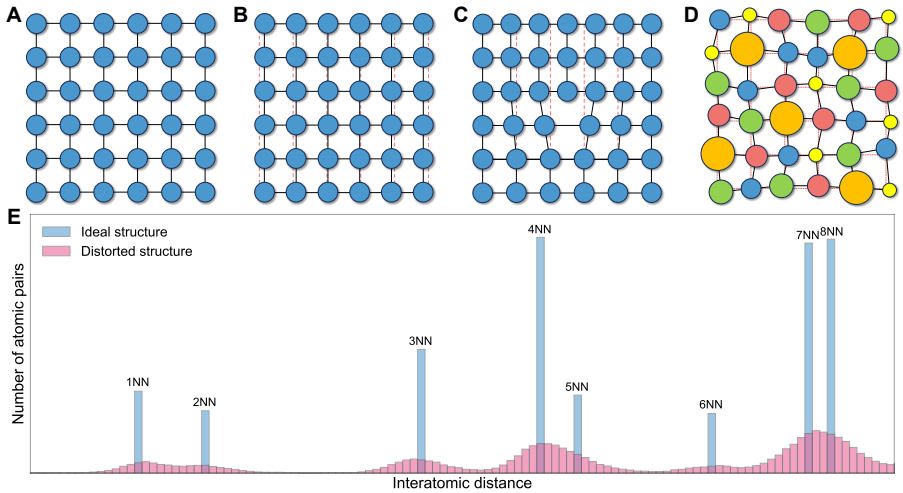

Figure 3.1: Schematic illustrations of different strain types in a 2D lattice, replotted after Owen et al. [29]. The black lines represent the actual lattice, the red dashed lines are the original/ideal lattice, and the circles are atoms, with different colours corresponding to different elements. (**A**) An ideal, strain-free structure. (**B**) Macrostrain, characterised by an integral change in inter-planar spacing. (**C**) Microstrain, shown by shifts in inter-planar spacing near defects. (**D**) lattice strains, leading to a localised distorted structure while maintaining an average structure. (**E**) The distribution of interatomic distances broadens in the distorted structure, where 1NN is the first nearest neighbour, 2NN the second and so on.

manifest as a broadened distribution of interatomic distances (bond lengths), as shown in Figure 3.1E; a phenomenon also observed in ab initio studies [30], [31], [32]. Therefore, the degree of broadening in the interatomic distance distribution, relative to a reference value, can serve as an indicator of lattice strain. This metric is particularly useful for comparing local structural changes across different materials from various experimental methods.

3.1.2 Static atomic displacements

As discussed in the previous section, lattice strains can be described as the degree of broadening in the distribution of interatomic distances. This broadening arises from the displacement of atoms from their ideal lattice positions as depicted in Figure 3.2. Figure 3.2A shows an ideal structure without displacement, where all atoms occupy their precise lattice sites. Introducing static displacements, i.e. LLDs, shifts atoms from their ideal positions, as shown in Figure 3.2B. At finite temperature, atoms also undergo vibrational motion, which leads to thermal displacements that cause the atomic positions to occupy a larger volume in space, though their time-average positions remain the same, as illustrated in Figure 3.2C.

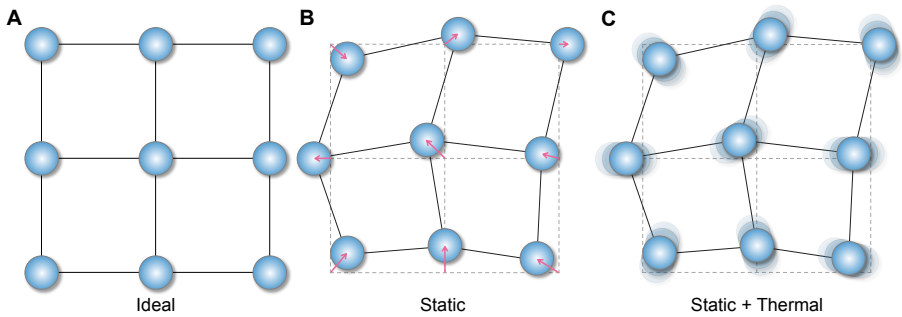

Figure 3.2: Schematic illustration of atomic off-site displacements in a 2D lattice. The blue balls represent atoms, solid lines represent actual lattice, dashed lines represent initial lattice. (**A**) Ideal lattice with no atomic displacements. (**B**) Static atomic displacements where atoms are displaced from their ideal lattice site with a length and direction indicated by the pink arrows. (**C**) Total atomic displacements where atoms vibrate around their displaced positions.

Here the methodology and terminology proposed by Owen et al. [33], [34] are adopted, in which static displacements are described as the statistical distribution of the atomic radii by the change in their standard deviation $\sigma_{\mathrm{s,u}}$ (here the subscript s indicates static displacements and u indicates off-site displacements), and LLDs ($\varepsilon_{\mathrm{s,u}}$) are calculated as the static displacements relative to average atomic radius $\bar{r}$:

$$\varepsilon_{\mathrm{s,u}} = \frac{\sigma_{\mathrm{s,u}}}{\bar{r}}. \tag{3.1}$$

Assuming a hard-sphere model for bcc-structured RHEAs, the average atomic radius $\bar{r}$ can be calculated from the lattice parameter a by $\bar{r} = \frac{\sqrt{3}}{4}a$.

In a highly symmetric bcc structure as in this case, static atomic displacements are isotropic and can be described by a Gaussian distribution:

$$f(u_{\mathrm{s,u}}) = \frac{1}{\sigma_{\mathrm{s,u}}\sqrt{2\pi}} \exp\left\{-\frac{1}{2}\left(\frac{u_{\mathrm{s,u}} - \mu_{\mathrm{s,u}}}{\sigma_{\mathrm{s,u}}}\right)^2\right\}, \tag{3.2}$$

where $u_{\mathrm{s,u}}$ is the static displacement and $\mu_{\mathrm{s,u}}$ is the mean. We assume that $\mu_{\mathrm{s,u}} = 0$ because when averaging over all atoms, the positive and negative displacements should cancel out without any net shift of the entire lattice.

Alternatively, one can define the statistical distribution of interatomic distances by the change in their standard deviation $\sigma_{\mathrm{s,l}}$ (here l refers to the interatomic distances), relative to the average bond length (μ_{l}):

$$\varepsilon_{\mathrm{s,l}} = \frac{\sigma_{\mathrm{s,l}}}{\mu_{\mathrm{l}}}. \tag{3.3}$$

Similarly the distribution of interatomic distances is given by:

$$f(u_{\mathrm{s,l}}) = \frac{1}{\sigma_{\mathrm{s,l}}\sqrt{2\pi}} \exp\left\{-\frac{1}{2}\left(\frac{u_{\mathrm{s,l}} - \mu_{\mathrm{l}}}{\sigma_{\mathrm{s,l}}}\right)^2\right\}. \tag{3.4}$$

The two are directly related as $\mu_{\mathrm{l}} = 2\bar{r}$ in the hard-sphere approximation. Additionally, since the two atoms involved in the bond length measurement each have their individual off-site displacements such that $\sigma^2_{\mathrm{s,l}} = \sigma^2_{\mathrm{s,u}} + \sigma^2_{\mathrm{s,u}}$, this means that $\sigma_{\mathrm{s,l}} = \sqrt{2}\sigma_{\mathrm{s,u}}$. In the following text, $\varepsilon_{\mathrm{s,u}}$ is used to represent the LLDs. Thus, σ_{s} and ε_{s} hereafter refer to $\sigma_{\mathrm{s,u}}$ and $\varepsilon_{\mathrm{s,u}}$, respectively.

3.2 Origin of LLDs

As LLDs arise from interactions between neighbouring atoms, two main factors are considered here: differences in interatomic distances and variations in bonding stiffness.

3.2.1 Interatomic distance difference

3.2.1.1 Atomic size mismatch

One commonly used quantitative definition is the atomic size mismatch (δ) defined by the deviation of the atomic radii of the individual elements from the mean radius:

$$\delta = \sqrt{\sum_i c_i \left(1 - \frac{r_i}{\bar{r}}\right)^2}, \bar{r} = \sum_i c_i r_i, \tag{3.5}$$

where c_i and r_i represent the concentration and atomic radius (metallic radii for 12-coordination are often adopted) of element i respectively, and $\bar{r}$ is the mean atomic radius. However, it has been shown that the magnitude of LLDs does not always correlate with the value of δ and alloys with comparable δ values can have substantial differences in LLDs [26], [30]. The atomic radius of a given element can vary depending on its local chemical environment, atomic sizes cannot be treated as fixed values across different systems. In addition, accurate determination of the actual atomic radii of constituent elements in HEAs is technically challenging, which complicates experimental quantification of LLDs.

3.2.1.2 Charge transfer effect

In the literature of HEAs, many have attributed the origin of LLDs exclusively to atomic size mismatch (δ) and use it to explain the effect of LLDs on properties. The issue here is that this attribution oversimplifies the structure of HEAs by relying on a hard-sphere model that ignores the effects of charge distribution and chemical bonding.

A more rigorous way to explain LLDs takes into account the effect of charge transfer, where constituent atoms can lose or gain electrons to vary their atomic sizes based on electronegativity differences during alloy formation. Charge transfer effect are more significant in bcc RHEAs which contain $3d$, $4d$ and $5d$ elements, in comparison with fcc HEAs composed mainly of $3d$ transition metals due to the larger electronegativity differences. As shown in Figure 3.3A

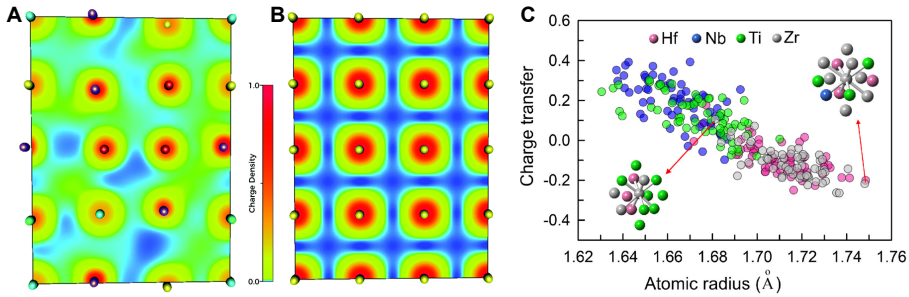

Figure 3.3: Electronic density maps of the (100) plane for (**A**) HfNbTiVZr and (**B**) Nb from DFT simulations. A delocalised electronic density and a distorted structure are observed in HfNbTiVZr. Different elements are coloured as follows: Hf–light blue, Nb–yellow, Ti–red, V–purple, Zr–green. *Reproduced from Ref. [35] with permission from the Chinese Chemical Society (CCS), Institute of Chemistry of Chinese Academy of Sciences (IC), and the Royal Society of Chemistry.* (**C**) Correlation between charge transfer in the *d* orbitals and atomic radius for HfNbTiZr, where a positive charge transfer value means electron gain while a negative value indicates electron loss. The local configurations illustrate that the extent of atomic size change depends on the local chemical environment, which results in size fluctuations for each element. *Reprinted from Ref. [36] with permission from Elsevier.*

and B, the electronic structure of a RHEA differs significantly from that of the pure element with the same crystal structure (bcc). In the RHEA, the electron density is delocalised, indicating significant charge transfer between the constituent elements, whereas the pure metal shows well-defined electron boundaries, suggesting there is no charge transfer. The charge transfer was also measured experimentally through core-level shifts using X-ray photoelectron spectroscopy [35].

Such charge transfer can lead to a significant reduction in LLDs. Tong et al. [26], [37] and Meng et al. [36] reported that atomic displacements are much smaller in the structural configuration generated by DFT simulations (which accounts for charge transfer) than in that obtained from reverse Monte Carlo (RMC) modelling, where atoms are treated as hard spheres (which don't consider charge transfer) despite both methods reproducing the experimental data with similar accuracy. This suggests that charge transfer can substantially reduce LLDs by as much as 80 % [37]. Specifically, as shown in Figure 3.3C, charge transfer occurs from larger atoms (Hf, Zr) to smaller atoms (Nb, Ti), consistent with the lower electronegativities of Hf and Zr compared to Nb and Ti. It should also be noted that the extent of charge transfer depends on the local chemical environments, which explains the distribution of atomic radii observed for each element in Figure 3.3C.

3.2.2 Force constant fluctuation

In the random solid solutions of HEAs, each atom has different neighbours, with some bonds being stiffer and others softer. This leads to unequal restoring forces, i.e. force constant fluctuations, which can shift atoms slightly and contribute to LLDs. Mu et al. [38] showed that in weak mass disorder alloys such as NiCo, NiFe, and NiFeCo, the force constant distributions are larger in NiFe and NiFeCo than in NiCo because of greater differences in chemical

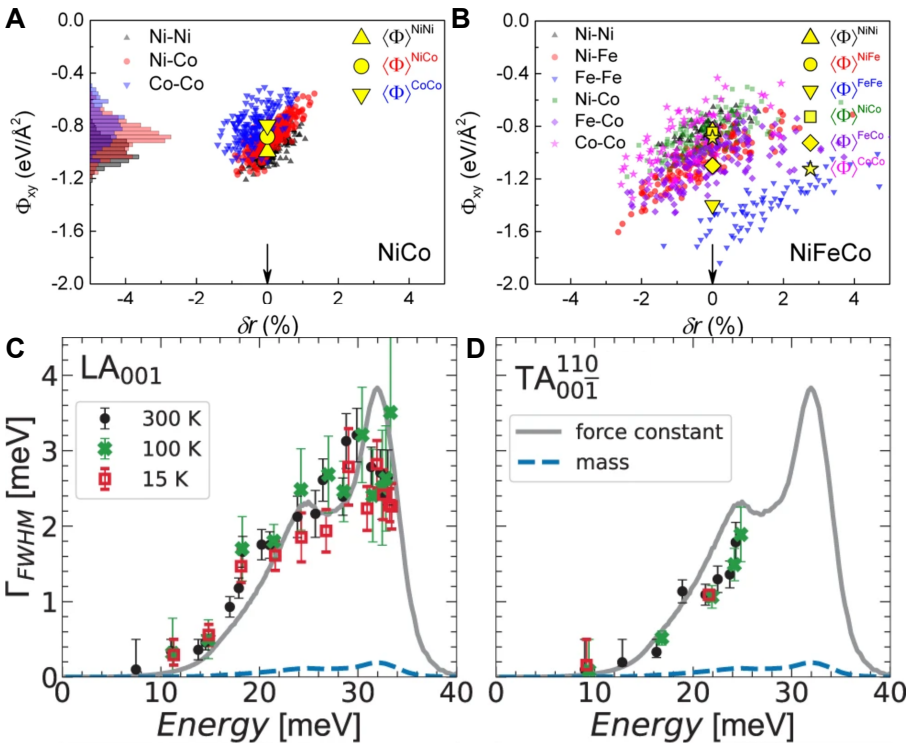

Figure 3.4: (**A**–**B**)The xy component of the nearest-neighbour force constant Φ_{xy} versus percent variation of the bond lengths, showing a larger force constant distribution in (**B**) NiFeCo than in (**A**) NiCo. *Reprinted from Ref. [38], licensed under a Creative Commons Attribution 4.0 International License. No changes were made.* (**C**–**D**) Phonon linewidths as a function of energy measured by inelastic X-ray scattering at 300, 100, and 15 K, and compared with a perturbation theory calculation of the broadening based on calculated mass fluctuations (blue dashed line) and estimated force constant fluctuations (grey solid line), for (**C**) longitudinal acoustic phonons propagating along [001] LA_{001} and (**D**) transverse acoustic phonons propagating along [00$\bar{1}$] and polarised along [110] $TA^{110}_{00\bar{1}}$. Force constant fluctuations have a strong effect on phonon broadening, especially for longitudinal modes. *Reprinted from Ref. [39], licensed under a Creative Commons Attribution 4.0 International License. No changes were made.*

bonding, as shown in Figure 3.4A and B. In addition, first-principles calculations reported strong phonon broadening at mid- to high frequencies in HEAs, partly due to force constant fluctuations [40]. Qualitatively, moving from left to right across the periodic table (e.g. from Hf over Ta to W) increases the interatomic bonding, resulting in increased force constants. Moving from top to bottom, the greater inner core charge enhances the local electronic density, which also leads to increased force constants. Similarly strong phonon broadening was also found in the fcc HEA CoCrFeMnNi through inelastic neutron and X-ray scattering experiments, again linked to scattering from force constant fluctuations [39] as shown in Figure 3.4C and D. As force constant fluctuations are expected to be larger in bcc RHEAs than in fcc alloys, their effect should not be neglected.

3.3 Effects of LLDs on properties of RHEAs

The effects of LLDs on RHEAs, particularly their influence on mechanical properties, have been reported in many studies. Wang et al. [7] linked the notable strengthening in $TiNbTaZrHf_{0.122}$ to lattice distortions that markedly impede dislocation movement. Lee et al. [41] identified lattice distortion as a key factor in solid solution strengthening in both NbTaTiV and NbTaTiVZr. By

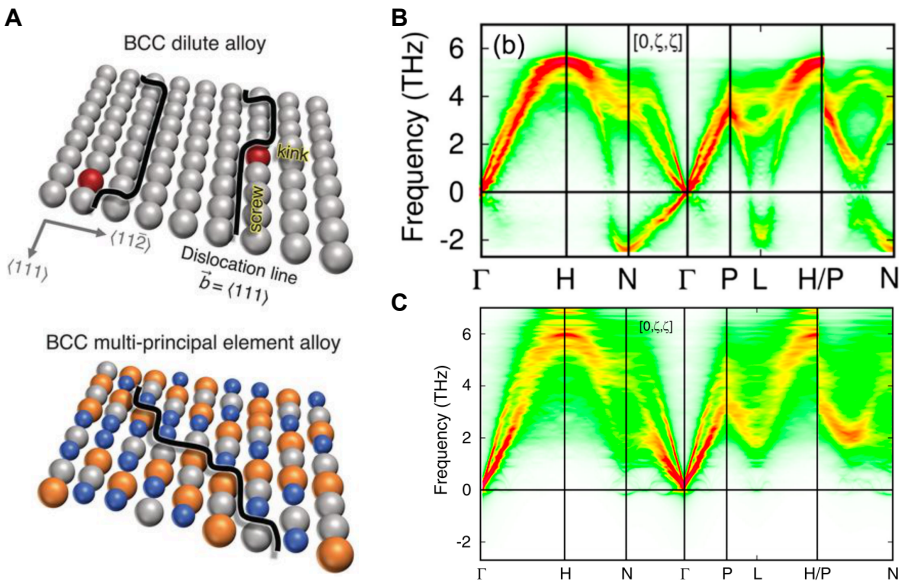

Figure 3.5: (**A**) Schematic of the dislocation morphologies in bcc dilute alloy and in bcc MPEA, respectively. *From Ref. [9]. Reprinted with permission from AAAS.* Calculated phonon dispersion of the bcc HfNbTiZr alloy, with (**B**) atoms occupying the perfect bcc lattice sites and (**C**) atoms in a fully relaxed bcc structure. *Reprinted figure with permission from Ref. [13] (https://doi.org/10.1103/PhysRevLett.126.025501) Copyright (2021) by the American Physical Society.*

comparing several alloys in the TiNbHfTaZr system, Thirathipviwat et al. [42] also reported a positive correlation between pronounced lattice distortion and increased solid solution strengthening. Furthermore, several studies suggest that LLDs may affect the motion of edge dislocations and contribute to enhanced strain hardening in bcc RHEAs [8], [9], [43], [44], as depicted in Figure 3.5A.

LLD has also been shown to stabilise the bcc phase in RHEAs. Density-functional theory (DFT) calculations indicate that, in addition to any entropic contributions, configurational disorder induced by LLDs provides an energetic stabilisation of the bcc phase through elimination of soft phonon modes [13]. This effect is evident by comparing Figure 3.5B with Figure 3.5C, where the instability showing by the negative phonon modes is eliminated through the inclusion of LLDs in the fully relaxed lattice. Borges et al. reported a similar finding, showing that LLDs reduce the magnitude of the structural energy differences and enhance the stability of the bcc phase [45].

Beyond mechanical and structural effects, other physical properties can also be affected by LLDs. Mu et al. [46] showed that LLDs can significantly modify the electronic density of states in several bcc RHEAs (HfNbTiZr, VCrZrNb, HfNbTaTiZr, and CrNbTiVZr), resulting in an increased electrical resistivity. A theoretical study by Jasiewicz et al. [47] revealed that the superconducting critical temperature in $(TaNb)_{0.67}(HfZrTi)_{0.33}$ decreases by about 50% when local distortions are introduced. Superconductivity has already been reported experimentally on $Hf_8Nb_{33}Ta_{34}Ti_{11}Zr_{14}$, a derivative of this RHEA [48] and other HfNbTaTiZr RHEAs [49]. LLDs can also reduce the lattice thermal conductivity through strong phonon scattering, which is one of the most effective routes for improving thermoelectric performance [50]. This concept of using configurational disorder to lower lattice thermal conductivity has also been applied to other thermoelectric materials such as chalcogenides [51].

3.4 Temperature dependence of LLDs

As discussed in Section 3.1.2, the overall atomic displacement is a superposition of static and thermal components, and it is challenging to completely separate them because of the temperature dependence of the thermal component. One approach is to measure the total displacement over a temperature range down to cryogenic, then linearly extrapolate to 0 K, at which point the thermal component is assumed to vanish, leaving the static part [52], [53]. Owen et al. [34] applied Debye model extrapolation which more accurately captures the low-temperature behaviour. However, both approaches assume that static displacements do not change with temperature. Lee et al. [54] studied bcc NbTaTiV at room and elevated temperatures and found that a compression yield strength of 688 MPa was retained at 900 °C (1273 MPa at room temperature). This strong resistance to high-temperature softening was ascribed to slow elemental diffusion induced by solid solution strengthening, which stems from lattice distortion during deformation. Controlling LLDs with temperature appears to be a promising route to optimise high-temperature mechanical properties in RHEAs, yet experimental information on the temperature dependence

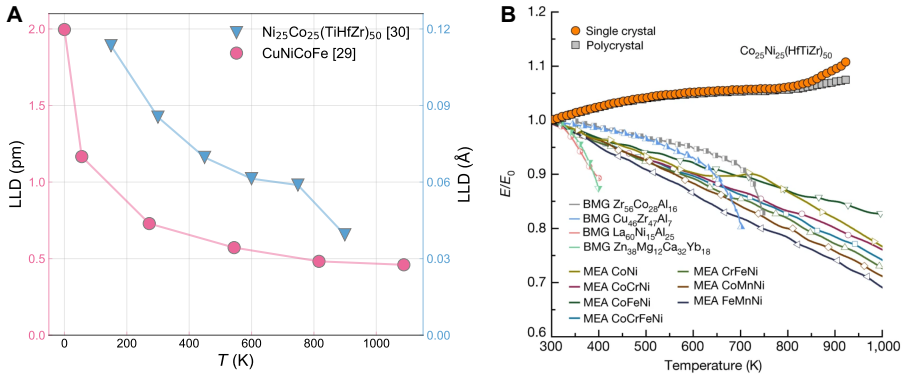

Figure 3.6: (**A**) LLDs decrease with temperature shown by molecular dynamics simulations for a fcc CuNiCoFe [55] and a B2 $Co_{25}Ni_{25}(HfTiZr)_{50}$ [56] HEA. (**B**) Relative change in Young's modulus (E/E_0, E_0 is Young's modulus at room temperature) with temperature for the $Co_{25}Ni_{25}(HfTiZr)_{50}$ HEA compared with other metallic materials, showing a favourable Elinvar effect [57]. *Reproduced with permission from Springer Nature.*

of LLDs is still lacking.

In fact, several molecular dynamics (MD) simulations have shown that LLDs decrease with temperature [55], [56], as seen in Figure 3.6A. This behaviour has been used to explain the increase in elastic moduli at high temperatures, which compensates for the decreased moduli caused by thermal expansion and leads to a temperature-insensitive elastic modulus (the Elinvar effect, shown in Figure 3.6B), and is useful in many industrial applications [57]. Based on this, a tunable Elinvar effect that correlates positively with lattice distortion can be achieved by controlling LLDs by means of their temperature dependence [58].

Therefore, experimental confirmation and a clear understanding of the temperature dependence of LLDs (in either trend) are important, not only for reconsidering the role of LLDs in high-temperature strengthening mechanisms but also for guiding the design of RHEAs for specific high-temperature applications.

Chapter 4

Measuring LLDs

Although simulation suggest that LLD may depend on temperature, experimental confirmation is still lacking. To investigate the temperature dependence of LLDs, these two components need to be separated. However, even at very low temperatures the thermal contribution cannot be fully removed because of zero-point energy. Assuming that LLDs are temperature-independent, a Debye-type analysis can still be applied, but the fundamental challenge remains that the measured displacements always contain a convolution of static and thermal components. This chapter introduces the approaches for measuring total atomic displacements and determining thermal displacements separately. Scattering-based methods are presented as the primary means for measuring total displacements, followed by several approaches for determining thermal vibrations including both simulations and direct experimental measurements.

4.1 Measurement of total atomic displacements

4.1.1 Elastic scattering

In this section, the use of scattering techniques to determine atomic structure is discussed, with a focus on elastic scattering. In elastic scattering, only momentum is transferred between the incident beam and the sample, while the energy (or the wavelength) of the scattered wave remains unchanged. Consider a beam incident on and subsequently be scattered by a sample, as shown in Figure 4.1. The incident and scattered beams are denoted as wave vectors $\mathbf{k}_i$ and $\mathbf{k}_j$, each with a magnitude of $2\pi/\lambda$ where λ is the wavelength of the beam. The scattering vector, or momentum transfer, $\mathbf{Q}$, is defined as

$$\mathbf{Q} = \mathbf{k}_j - \mathbf{k}_i, \tag{4.1}$$

where $k_j = k_i$. From $\mathbf{Q}$ the scattering amplitude $\Psi(\mathbf{Q})$ is defined as:

$$\Psi(\mathbf{Q}) = \frac{1}{\langle b \rangle} \sum b \mathrm{e}^{\mathrm{i}\mathbf{Q}\cdot\mathbf{R}}, \tag{4.2}$$

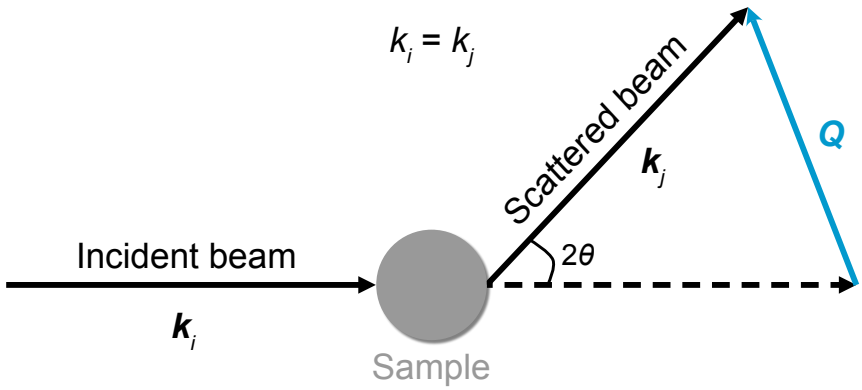

Figure 4.1: A 2D schematic illustration of elastic scattering from a sample. The incident beam has wavelength λ and wave vector $\mathbf{k}_i$, and the scattered beam has wave vector $\mathbf{k}_j$, where $k_j = k_i$. $\mathbf{Q} = \mathbf{k}_j - \mathbf{k}_i$ is the scattering vector and 2θ is the scattering angle.

where b is the scattering length. For X-rays, b depends on Q, but for neutrons b is independent of Q. The angle brackets denote the average value. $\mathbf{R}$ is the atomic position. However, scattering amplitude is not measurable in practice. Instead, what is measured in an experiment is the scattering intensity, which is related to the differential scattering cross section from the square of the magnitude of $\Psi(\mathbf{Q})$:

$$\frac{\mathrm{d}\sigma(\mathbf{Q})}{\mathrm{d}\mathbf{\Omega}} = \frac{\langle b \rangle^2}{N} |\Psi(\mathbf{Q})|^2 = \frac{1}{N} \sum_{i,j} b_i b_j \mathrm{e}^{\mathrm{i}\mathbf{Q}\cdot(\mathbf{R}_i - \mathbf{R}_j)}, \tag{4.3}$$

where σ is the total number of scattered particles (neutrons or photons in the case of X-rays), $\mathbf{\Omega}$ the solid angle in 3D space, $\frac{\mathrm{d}\sigma(\mathbf{Q})}{\mathrm{d}\mathbf{\Omega}}$ denotes the number of particles scattered into solid angle per second from all incident particles, N is the number of individual scatterers (atoms) in the gauge volume, and i and j refer to different atoms. The scattering intensity $I(\mathbf{Q})$ is a normalised form of the differential cross section:

$$I(\mathbf{Q}) = \frac{\mathrm{d}\sigma(\mathbf{Q})}{\mathrm{d}\mathbf{\Omega}} + \langle b \rangle^2 - \left\langle b^2 \right\rangle = \langle b \rangle^2 S(\mathbf{Q}), \tag{4.4}$$

where $S(\mathbf{Q})$ is the scattering structure function,

$$S(\mathbf{Q}) = \frac{I(\mathbf{Q})}{\langle b \rangle^2}. \tag{4.5}$$

4.1.1.1 Diffraction

If the sample is crystalline, constructive interference occurs when the Laue condition is fulfilled, defined as:

$$\mathbf{Q} = \mathbf{G}, \tag{4.6}$$

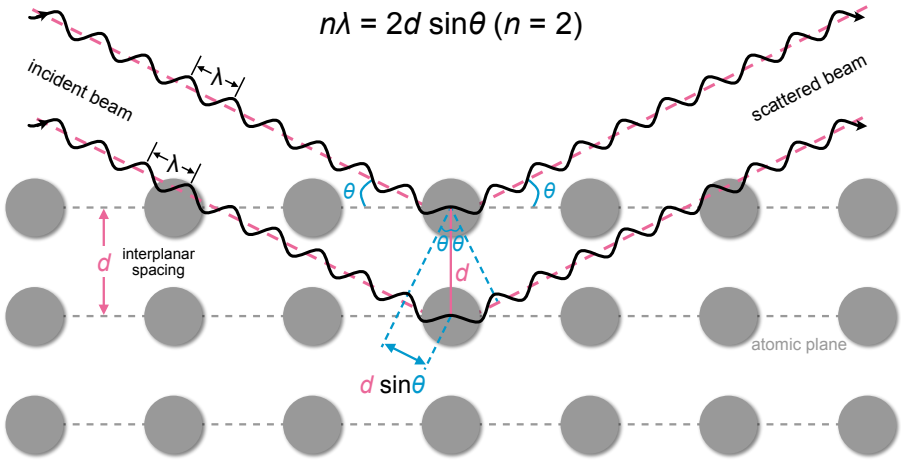

Figure 4.2: Schematic illustration of Bragg's law. A parallel beam with wavelength λ is incident from the left onto a set of atomic planes with interplanar spacing d and incident angle θ. The extra path travelled by the lower beam equals to an integer multiple (2 in this case) of the wavelength, satisfying the Bragg condition.

where $\mathbf{G}$ is a reciprocal lattice vector with magnitude $|\mathbf{G}| = 2\pi/d$. For elastic scattering, the magnitude of the incident and scattered wavevectors are equal, $|\mathbf{k}_i| = |\mathbf{k}_j| = 2\pi/\lambda$, which leads to:

$$Q = \frac{4\pi \sin\theta}{\lambda}. \tag{4.7}$$

Combining this with $|\mathbf{G}| = Q$ gives:

$$n\lambda = 2d \sin\theta, \tag{4.8}$$

where n is an integer, λ is the wavelength of the incident wave, and d is the interplanar spacing. This scalar relation is the well-known *Bragg's Law*. When it is satisfied, constructive interference produces the intense peaks observed in 1D diffraction patterns at the scattering angle θ, as illustrated in Figure 4.2. Bragg's law is a special case of the Laue condition.

For a well-crystalline sample, scattering appears as sharp Bragg peaks in the pattern, with background intensity underneath the peaks. This background arises from instrumental imperfections, fluorescence, multiple scattering and diffuse scattering and other phenomena. In practice, the background can complicate interpretation of the diffraction pattern and is usually removed by fitting a polynomial function to isolate the Bragg peaks.

4.1.1.2 Diffuse scattering

Traditional crystallography assumes that crystals are composed of a three-dimensional repetitive lattice of identical units and all the structural information

is contained in the diffraction peaks. However, real-world materials often deviate from this idealised model, and their diffraction patterns commonly include more than just sharp Bragg peaks. As discussed in the previous section, diffraction captures only a specific part of the scattering where constructive interference happens. Waves are also scattered out of phase due to the imperfect structure of the material and contribute to the intensity, which is known as diffuse scattering.

Diffuse scattering spans the entire Q range and usually appears as a weak, continuous background, in contrast to Bragg diffraction which occurs exclusively at specific points where the Bragg condition is satisfied (Equation (4.8)). Diffuse scattering is indicative of any deviations from the perfect crystal structure. While Bragg diffraction provides information about the average structure, many material properties are strongly affected by the structural imperfections or local disorder that are captured through diffuse scattering. Although diffuse scattering has been studied since the beginning of crystallography, it has mainly been explored by a small number of specialised groups due to its low signal intensity and the difficulty in data interpretation. Nevertheless, the development of synchrotron radiation and neutron sources, high-resolution and wide-coverage detectors, and improved computational tools for analysis and modelling have significantly reduced many of the difficulties that previously limited progress in diffuse scattering studies.

4.1.1.3 Total scattering

Total scattering is a technique that combines the information of both long-range order from Bragg peaks (average structure) and local disorder from diffuse scattering. The total scattering and pair distribution function (PDF) nomenclatures used in this thesis are mainly from Egami and Billinge [59]. Based on the scattering structure function defined in Equation 4.5, the reduced structure function $F(Q)$ is defined as:

$$F(Q) = Q[S(Q) - 1]. \tag{4.9}$$

By applying a sine transform to $F(Q)$, the reduced pair distribution function can be derived from reciprocal-space data, transforming the information from reciprocal space into real space:

$$G(r) = \left(\frac{2}{\pi}\right) \int_0^\infty F(Q) \sin(Qr) \mathrm{d}Q. \tag{4.10}$$

However, reaching zero or infinity in Q is not feasible in practical experiments. So the equation is modified to account for the limited range of Q:

$$G(r) = \left(\frac{2}{\pi}\right) \int_{Q_{\min}}^{Q_{\max}} F(Q) \sin(Qr) \mathrm{d}Q, \tag{4.11}$$

The reduced pair distribution function $G(r)$ can also be defined in terms of the pair density function:

$$G(r) = 4\pi r \left[\rho(r) - \rho_0\right] = 4\pi r \rho_0 [g(r) - 1], \tag{4.12}$$

where $\rho(r)$ is the atom-pair density function, $g(r)$ is the pair distribution function derived from the Fourier transform of the structure function $S(Q)$, and ρ_0 is the atomic number density of N atoms in the volume V ($\rho_0 = N/V$).

In multicomponent systems, which comprise more than one type of atom and represent the majority of practical cases, the calculation of the reduced pair distribution function $G(r)$ requires a modification [59]:

$$G(r) = \sum_{\alpha}\sum_{\beta} W_{\alpha\beta} G_{\alpha\beta}(r) = 4\pi r \rho_0 \sum_{\alpha}\sum_{\beta} [g_{\alpha\beta}(r) - 1], \tag{4.13}$$

where $G_{\alpha\beta}(r)$ is the partial reduced pair distribution function,

$$W_{\alpha\beta} = c_\alpha c_\beta \frac{b_\alpha b_\beta}{\langle b \rangle^2}, \tag{4.14}$$

is the weighting, and the measured PDF is the weighted sum of the different partial PDFs.

It is worth noting that $G(r)$ is often normalized further to remove the scaling arising from the atomic concentrations and scattering lengths. Moreover, different formalisms are used in different softwares. To avoid confusion, a comprehensive comparison of these normalisations and formalisms is provided in Ref. [60].

4.1.1.4 Pair distribution function

The pair distribution function (PDF) is a histogram of the distribution of interatomic distances, weighted by scattering length, as schematically illustrated in Figure 4.3. Peaks in the PDF correspond to different interatomic distances or atomic shells. The first, second and third shells in a bcc lattice are marked in

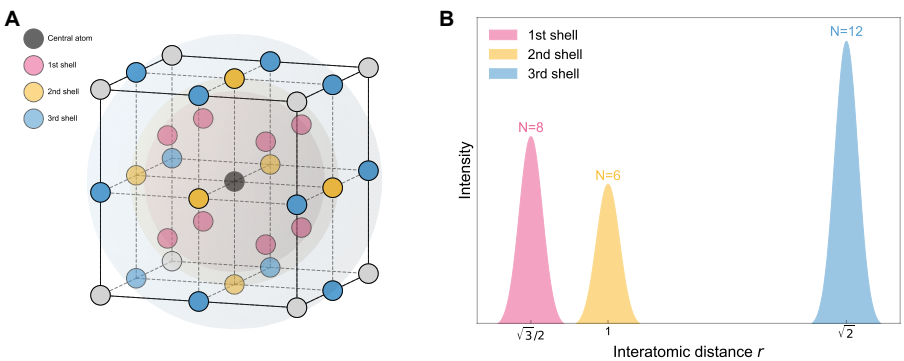

Figure 4.3: Schematic illustration of **(A)** a bcc lattice showing the first three nearest-neighbour atomic shells composed of eight unit cells, where red spheres represent the first shell (body-centred atoms), yellow spheres the second shell (corner atoms), and blue spheres the third shell (corner atoms). **(B)** The corresponding PDF, with peak intensity reflecting coordination numbers and peak widths, have been exaggeratedly broadened for visualisation purpose.

red, yellow and blue, respectively, in Figure 4.3A, surrounding a central atom (black). Figure 4.3B illustrates a theoretical PDF, where the peak positions indicate bond lengths (r), while the peak intensities reflect the coordination numbers, i.e., the number of neighbouring atoms at each distance. The peak widths reflect the variation in bond lengths, so if all atoms were positioned at their ideal lattice sites, the peaks would be delta functions. The magnitude of the peak broadening can be used to quantify off-site atomic displacements.

Historically, PDF analysis was primarily used to characterise disordered materials, with limited application in the study of crystalline systems. However, the advent of synchrotron X-ray radiation and spallation neutron sources has markedly improved the data quality over a wide Q range, which gives a better resolution in real space according to Equation (4.11). This enhancement has made PDF analysis a powerful tool for probing atomic-scale disorder. Total scattering and PDF analysis are bulk techniques that especially provide information on local structures over longer length scales compared to other techniques, which allows for a more complete picture of the material's atomic structure.

4.1.1.5 Effect of atomic displacements on scattering

The method for measuring total atomic displacements using a scattering-based technique is based on how these displacements affect the scattering signal. In general, atomic displacements lead to intensity decay in diffraction patterns (reciprocal space) and peak broadening in the PDF (real space).

The off-site displacement of an atom could be considered as a deviation ($\mathbf{u}$) of the atomic position from the average position $\bar{\mathbf{R}}$, where $\mathbf{R} = \bar{\mathbf{R}} + \mathbf{u}$. Equation (4.3) is now:

$$\frac{\mathrm{d}\sigma(\mathbf{Q})}{\mathrm{d}\boldsymbol{\Omega}} = \frac{1}{N}\sum_{i,j} b_i b_j e^{i\mathbf{Q}[(\bar{\mathbf{R}}_i+\mathbf{u})-(\bar{\mathbf{R}}_j+\mathbf{u})]}. \tag{4.15}$$

For simplicity, deriving only the exponential part, Equation (4.15) is reduced to

$$e^{i\mathbf{Q}\bar{\mathbf{R}}_i[1+i\mathbf{Q}\mathbf{u}-\frac{1}{2}(\mathbf{Q}\mathbf{u})^2+\ldots]-i\mathbf{Q}\bar{\mathbf{R}}_j[1+i\mathbf{Q}\mathbf{u}-\frac{1}{2}(\mathbf{Q}\mathbf{u})^2+\ldots]} \approx e^{i\mathbf{Q}(\mathbf{R}_i-\mathbf{R}_j)} \cdot e^{-\mathbf{Q}^2\mathbf{u}^2}, \tag{4.16}$$

where $e^{-\mathbf{Q}^2\mathbf{u}^2} = e^{-2W}$, e^{-W} is the Debye-Waller factor. A common way to write this is:

$$e^{-\mathbf{Q}^2\mathbf{u}^2} = e^{-2B(\frac{\sin\theta}{\lambda})^2}, B = 8\pi^2 u^2. \tag{4.17}$$

In the harmonic approximation, thermal displacements can be described by a Gaussian distribution as:

$$f(u_{\mathrm{thermal}}) = \frac{1}{\sigma_{\mathrm{thermal}}\sqrt{2\pi}} \exp\left\{-\frac{1}{2}\left(\frac{u_{\mathrm{thermal}} - \mu_{\mathrm{thermal}}}{\sigma_{\mathrm{thermal}}}\right)^2\right\}, \tag{4.18}$$

where u_{thermal} is the thermal displacement and $\mu_{\mathrm{thermal}} = 0$ is the mean, and $\sigma_{\mathrm{thermal}}$ is the standard deviation. Similarly, as shown in Equation 3.2, static displacement is also described by a Gaussian distribution with the standard

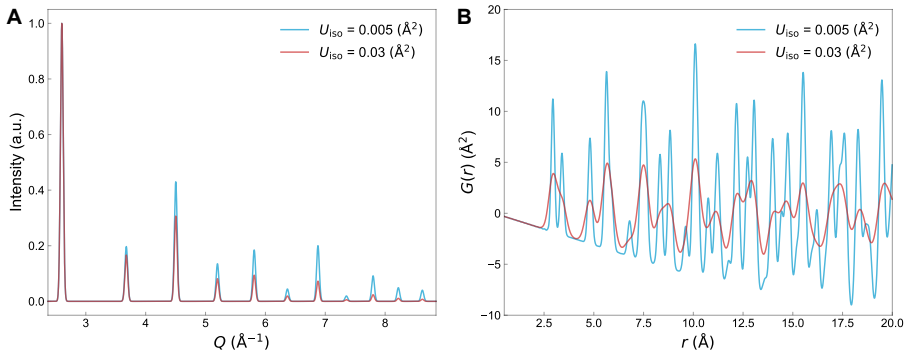

Figure 4.4: Simulated (**A**) diffraction patterns and (**B**) PDFs for two bcc structures with smaller (0.005 Å^2) and larger (0.03 Å^2) U_{iso} values. In the diffraction patterns, the larger U_{iso} results in decaying peak intensity, while in the PDFs it leads to peak broadening.

deviation σ_{static}. In a highly symmetric bcc structure, atomic displacements are the same in all directions and can be described by an isotropic atomic displacement parameter (ADP) U_{iso}, which is essentially the mean-square displacement $\langle u^2 \rangle$. Under this approximation, atomic displacements follow a Gaussian distribution where the standard deviation σ is equal to the square root of the mean-square displacement, i.e. $\sigma = \sqrt{\langle u^2 \rangle}$, and thus $U_{\text{iso}} = \langle u^2 \rangle = \sigma^2$. The same applies to thermal and static components, i.e. $\sigma^2_{\text{thermal}} = U_{\text{thermal}}$ and $\sigma^2_{\text{static}} = U_{\text{static}}$. Since the total displacement is a convolution of these two contributions, $\sigma^2 = \sigma^2_{\text{thermal}} + \sigma^2_{\text{static}}$, and equivalently, $U_{\text{iso}} = U_{\text{thermal}} + U_{\text{static}}$. However, real-world experimental determination of U_{iso} also contains artefacts from instrument limitations (e.g., resolution, calibration) and approximations in the data processing, which are treated as an additive component to U_{iso}:

$$U_{\text{exp}} = U_{\text{iso}} + U_{\text{i/p}} = U_{\text{thermal}} + U_{\text{static}} + U_{\text{i/p}}, \tag{4.19}$$

where U_{exp} is the experimentally determined value and $U_{\text{i/p}}$ is the instrument/processing component; the latter will be further discussed in Section 4.3. U_{exp} can be obtained from scattering experiments, either through Rietveld refinements of reciprocal-space diffraction data, or from real-space small-box fitting of PDFs. More details of these two data analysis methods are presented in Chapter 5.

In reciprocal-space diffraction, atomic displacements lead to a Q-dependent decay of peak intensity as shown in Figure 4.4A. This decay is described by the form factor f:

$$f = f_0 \exp\left(-\frac{Q^2 U_{\text{exp}}}{2}\right), \tag{4.20}$$

where f_0 is the atomic scattering factor. For X-rays, f_0 is proportional to the electron density and therefore to Q, whereas for neutrons it is proportional to coherent neutron scattering length b. Because neutron scattering lengths do

not change with Q in the same way as X-ray form factor, neutron scattering is generally more suitable for determining atomic displacements.

In real-space PDFs, increase in U_{exp} leads to an increase in the peak width $\sigma(r)$, as shown in Figure 4.4B. This phenomenon is mathematically modelled in the PDF fitting software PDFgui [61], [62] as:

$$\sigma(r) = \sqrt{U_{\text{exp}} \left(1 - \frac{\delta_1}{r} - \frac{\delta_2}{r^2} + Q_{\text{broad}}^2 r^2\right)}, \tag{4.21}$$

where r is the interatomic distance, δ_1 and δ_2 are correction factors for peak narrowing at small r values, addressing the effects of correlated motion, and the term Q_{broad} accounts for the superposition of PDF peaks due to a spread in the incident neutron wavelength, which is introduced by the finite sample's width.

4.1.2 Other techniques

4.1.2.1 TEM

Transmission Electron Microscopy (TEM) is a sophisticated tool for investigating the microstructure of materials at high spatial resolution that enables direct observation of local strains at atomic length scales. Among the TEM-based methods for strain measurement, dark field electron holography offers high precision [63], but it is strongly affected by sample thickness and requires a strain-free reference area, making it less suitable for studying LLDs in HEAs. Li et al. reported high-angle annular dark-field scanning TEM (HAADF-STEM) images of CoCrFeMnNi free of defects, and calculated lattice strains using the geometric phase analysis method [64]. Direct TEM imaging also includes high-resolution TEM (HRTEM), which provides exceptional spatial resolution ($\sim$ 0.03 Å) [65], yet it is also sensitive to sample thickness and may introduce artefacts. Nanobeam electron diffraction (NBED) avoids the need for a reference area [66], [67], but its accuracy can be limited by nonuniform intensity of the diffraction spots and reduced spatial resolution ($\sim$ 1 nm). A significant concern for these TEM techniques is the necessity for sample thinning, which may relax the material, thereby reducing the original level of strain. Hÿtch et al. [68] proposed that the thinning process introduces two free surfaces that are not present in the bulk sample, which can relax some of the strain, typically by about 10 %. Hence, for HEAs where accurate stain analysis requires the measurements to be bulk-representative, these limitations make TEM-based methods less ideal.

4.1.2.2 EXAFS

Extended X-ray absorption fine structure (EXAFS) is also widely used for probing local structure. A key advantage of EXAFS is it provides element-specific information of the local coordination environment, which makes it possible to measure LLDs [69], [70]. Tan et al. reported a pronounced LLD of 5.2% around Zr-center, larger than the 4% around Nb-center in a HfNbTaTiZr

RHEA [71]. However, this specificity can also introduce challenges, especially in HEAs, where multiple elements are involved. Each element requires a separate measurement, which complicates the experiments. Another issue is that in HEAs, the absorption edges of the constituent elements might be closely spaced in energy if their electronic structures are similar. If these challenges can be managed, EXAFS can be used to determine the distribution of bond lengths around different atomic species and subsequently the quantification of LLDs. For instance, Fantin et al. reported a LLD value of around 1% in MoNbTaW [72], [73].

4.2 Determination of thermal displacements

4.2.1 Rule-of-mixture estimation

Experimental determination of thermal displacements typically requires either variable-temperature measurements or molecular dynamics simulations, but they are not always feasible because of the requirement of specialised instruments or significant computational resources, and can be time-consuming. So, alternative estimation methods are often needed when direct measurements or simulations are not available.

A simple way to estimate thermal displacements is applying the rule-of-mixture (ROM), where the thermal displacement parameter (U_{thermal}) is approximated from individual elements in the alloy at temperature T, given by:

$$U^T_{\text{thermal}} = \sum_i c_i U^T_i, \tag{4.22}$$

where c_i is the concentration and U^T_i the displacement parameter of pure element i at temperature T. c_i can be determined from chemical composition, and U^T_i can be determined from the Debye-Waller factor according to Equation 4.17:

$$U^T_i = \frac{B^T_i}{8\pi^2}, \tag{4.23}$$

where B^T_i is the B-factor of element i at temperature T.

4.2.2 Vibrational density of states

Thermal displacements originate from the thermal vibration of atoms in a crystal, which can be quantified. Similar to how light, a wave motion, can be viewed as particles (photons), the thermal vibrations of atoms in a crystal can also be viewed as waves that are quantised into phonons. Phonons represent the vibrational modes of the lattice, and the distribution of these modes as a function of frequency/energy is described by the vibrational density of states (VDOS). The thermal displacement parameter U_{thermal}, which is essentially the mean-square thermal atomic displacement $\langle u^2_{\text{thermal}} \rangle$, can be obtained by integrating the VDOS weighted by the inverse frequency and the Bose-Einstein

occupation factor:

$$U^i_{\text{thermal}} = \frac{\hbar}{4\pi M}\int_0^\infty \frac{g(f)}{f}\left[2n(f,T)+1\right]\mathrm{d}f, \tag{4.24}$$

where $\hbar$ is the reduced Planck constant, M is the molar mass of material, f is the ordinary frequency with unit Hz ($f = \frac{\omega}{2\pi}$, ω is the angular frequency), $g(f)$ is the VDOS and n is the Bose-Einstein occupation factor

$$n = \frac{1}{e^{\frac{hf}{k_\mathrm{B}T}} - 1}, \tag{4.25}$$

where h is the Planck constant and k_B is the Boltzmann constant.

The VDOS can be obtained from molecular dynamics (MD) simulations, in which partial VDOS for each constituent element in an RHEAs can be calculated separately. The total VDOS is then obtained by summing the partials weighted by the molar mass and atomic fraction of each element. MD-based VDOS remains one of the preferred methods for determining thermal displacements in this work. The MD simulations were performed by collaborators, and therefore only the results obtained from the simulations (not the simulation methodology itself) will be discussed in this thesis.

To allow direct comparison with U_{iso} from neutron scattering, we must account for the differences in neutron coherent scattering length, b_i, between the elements, and each U^i_{thermal} is therefore weighted when calculating the total $U^{\text{VDOS}}_{\text{thermal}}$ as:

$$U^{\text{VDOS}}_{\text{thermal}} = \frac{\sum_i w_i U^i_{\text{thermal}}}{\sum_i w_i}, \tag{4.26}$$

where the weights are given by $w_i = c_i b_i^2$.

4.2.3 Debye approximation and specific heat

In the absence of complete VDOS information, the Debye approximation is sometimes used to estimate the integral vibrational properties of crystals, such as the specific heat or the atomic thermal displacement [74], [75]. The approximation ignores the existence of the optic branches of the phonon spectrum, and assumes a linear dispersion relation with an average sound velocity for the three acoustic branches.

The Debye approximation gives values for the specific heat $C_\mathrm{v}^{\text{Debye}}$ (the subscript v indicates a constant volume), which has been proved to be in reasonable agreement with experiments, especially at low temperatures, described by:

$$C_\mathrm{v}^{\text{Debye}} = 9R\left(\frac{T}{\Theta_\mathrm{D}}\right)^3 \int_0^{\Theta_\mathrm{D}/T} \frac{x^4 \mathrm{e}^x}{(\mathrm{e}^x-1)^2}\,\mathrm{d}x, \tag{4.27}$$

where R is the gas constant, Θ_D is the Debye temperature, and $x = \hbar\omega/k_\mathrm{B}T$. The Debye approximation also gives values for the mean-square atomic dis-

placement:

$$U_i^{\text{Debye}} = \langle u_i^2 \rangle = \frac{3\hbar^2}{\bar{M} k_{\text{B}} \Theta_{\text{D}}} \left(\frac{1}{4} + \left(\frac{T}{\Theta_{\text{D}}} \right)^2 \int_0^{\Theta_{\text{D}}/T} \frac{x}{\mathrm{e}^x - 1} \, \mathrm{d}x \right), \tag{4.28}$$

adding neutron scattering length weighting,

$$U_{\text{thermal}}^{\text{Debye}} = \frac{\sum_i w_i U_i^{\text{Debye}}}{\sum_i w_i}. \tag{4.29}$$

The specific heat is one of the easiest thermodynamic quantities to measure experimentally. By fitting the Debye model to the measured specific heat using Equation (4.27), a Debye temperature can be obtained. This value can then be used in Equation (4.28) to calculate the atomic displacements arising from thermal vibrations, i.e., the thermal displacements. It should be noted that the harmonic approximation does not allow for thermal expansion, so Equation (4.27) is only applicable under constant volume. However, all experiments are performed under constant pressure, since preventing thermal expansion experimentally is nearly impossible. A simple conversion between the specific heat at constant pressure C_{p} and at constant volume C_{v} is:

$$C_{\text{p}} = C_{\text{v}} + \alpha^2 B V T, \tag{4.30}$$

where α is the thermal expansion coefficient, B is the bulk modulus and V is the molar volume.

4.3 Determination of instrument/processing component

The last part to consider is the component from the instrument and data processing $U_{\text{i/p}}$, as described in Equation (4.19). $U_{\text{i/p}}$ was determined using a reference sample that is free from static displacement, in this case a bcc pure metal Nb. The reference sample was measured over a range of temperatures under identical experimental conditions as the studied RHEAs, and subjected to the same data processing. Here two approaches were used to determine $U_{\text{i/p}}$:

- For analyses where thermal displacements are determined through VDOS: it is approximated that at temperature above 50 K the contribution from zero-point motion becomes negligible and U_{iso} varies approximately linearly with temperature. The U_{iso} values measured down to 50 K are extrapolated to 0 K, and the intercept of this fitted line is taken as the contribution from the instrument and data processing.

- For analysis where thermal displacements are determined through the Debye model: the U_{iso} values of Nb are fitted using the Debye model with an added constant offset. This offset accounts for $U_{\text{i/p}}$.

Chapter 5

Experiments and data processing

5.1 Materials and microstructure

5.1.1 Heterogeneous RHEAs powder

To prepare HfNbTaTiZr in the form of gas atomised powders, first, ingots of the initial HfNbTaTiZr alloy were produced by arc-melting of blends of pure metals with $>$ 99.9 wt.% purity and placed in a water-cooled copper crucible, under a protective He atmosphere. To mix the elements in the melt pool properly and to homogenise the produced material, the ingot was flipped and repeatedly remelted a total of eight times. The ingots were subsequently gas atomised into powder by electrode induction-melting gas atomisation in a crucible-free process under a protective Ar atmosphere to suppress undesirable oxidation of the material. The particle size distribution of the final powder is 17–277 μm (Dv10-Dv90). Each powder particle contains numerous equiaxed grains, and the average diameter of these grains is 9.5 $\pm$ 2.9 μm [27]. NbTaTiZr and MoNbTaW powders were also produced following a similar route.

The microstructure of the powder was characterised using energy-dispersive X-ray spectroscopy (EDS) in a scanning electron microscope (FEI Quanta 200 FEG ESEM operated at 10–20 kV). Back-scatter electron (BSE) imaging was performed at 10–15 kV to obtain high resolution chemical contrast. BSE images of the microstructure and the corresponding EDS maps for HfNbTaTiZr, NbTaTiZr and MoNbTaW are shown in Figure 5.1. Dendritic microstructures can be clearly observed in HfNbTaTiZr and NbTaTiZr, while MoNbTaW has much less segregation. This is similar to the as-cast material as shown in Figure 2.3. The chemical composition was determined by EDS analysis and is listed in Table 5.1. Significant variations in elemental composition are observed between dendrites and interdendritic regions of HfNbTaTiZr, with enrichment of Nb and Ta in the dendrites while Hf, Ti, and Zr, which have relatively lower melting points, are more abundant in the interdendritic regions. The segregation is the same as reported by Tong et al. [26] and other studies [27], [76], but the

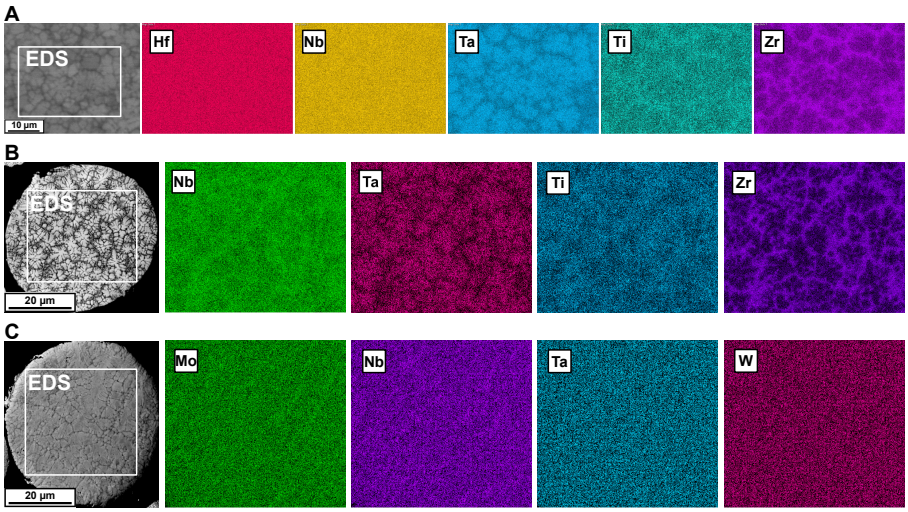

Figure 5.1: Dendritic microstructure of (**A**) HfNbTaTiZr, (**B**) NbTaTiZr and (**C**) MoNbTaW powder sample shown by BSE SEM and EDS.

Table 5.1: Chemical composition in atomic percent (at.%) of RHEAs powder from EDS.

Alloy	**Hf**	**Mo**	**Nb**	**Ta**	**Ti**	**W**	**Zr**
HfNbTaTiZr	20.49(6)		19.0(2)	20.3(5)	22.3(2)		17.9(5)
Dendrite	19.0(3)		21.6(4)	27.9(6)	18.8(5)		12.7(4)
Interdendrite	21.0(4)		15.1(6)	11(1)	27.4(8)		25(1)
NbTaTiZr			23.6(3)	22.7(9)	24.7(6)		29(1)
Dendrite			30(4)	33(4)	20(3)		17(3)
Interdendrite			17(6)	12(4)	29(5)		42(6)
MoNbTaW		23(1)	25(2)	24(2)		28(1)	
Dendrite		25(4)	23(3)	25(4)		27(4)	
Interdendrite		25(7)	33(7)	23(6)		19(8)	

magnitude of the chemical differences is larger in the present material due to the rapid solidification associated with the gas atomisation process.

5.1.2 Homogeneous HfNbTaTiZr solid

Experimental determination of atomic displacements includes artefacts from chemical heterogeneity, microstrain, and preferred orientation. These influences can be minimised through careful sample preparation aiming for a homogeneous

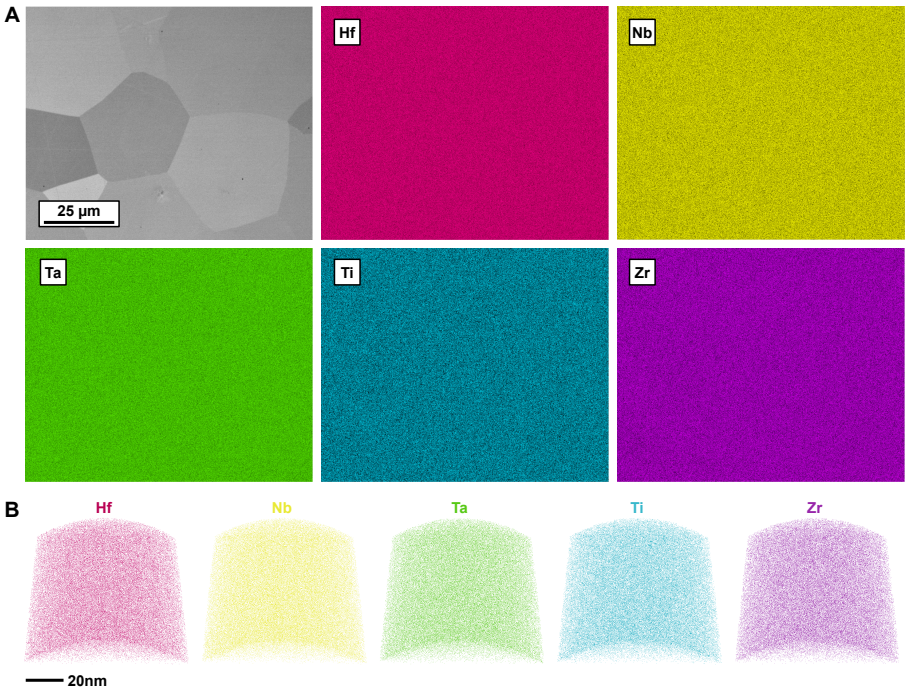

Figure 5.2: (**A**) BSE image and EDS maps of HfNbTaTiZr bulk sample. (**B**) Reconstructions from atom probe tomography (APT). Both confirm a homogeneous microstructure in HfNbTaTiZr.

Table 5.2: Chemical composition in atomic percent (at.%) of homogeneous HfNbTaTiZr from EDS.

Element	**Hf**	**Nb**	**Ta**	**Ti**	**Zr**
Composition (at.%)	20.86(5)	20.41(9)	20.22(3)	19.2(1)	19.31(5)

and annealed material that approximates a strain-free crystallographic powder [29]. This was achieved for HfNbTaTiZr by using large gauge volumes of a chemically homogeneous material.

The homogenised bulk sample was prepared through spark plasma sintering (details described in Ref. [27]). This process produced four bulk cylinders, each with a height of 10 mm and a diameter of 10 mm—dimensions that fit into the neutron scattering experiment sample cans. BSE imaging was performed at 5 kV and EDS map scans were taken at 15 kV. The BSE image and EDS maps are shown in Figure 5.2A, where all elements, as listed in Table 5.2, are homogeneously distributed. The homogeneity of the sample was additionally investigated at the nanoscale via atom probe tomography (APT). APT specimens were prepared via focused ion beam (FIB) in a dual-beam FEI Versa 3D workstation implementing well-known procedures for sample lift-out

and preparation ([77], [78]). The specimens were measured on a CAMECA LEAP 6000 XR in laser-mode. The specimen was run at a temperature of 50 K, using laser pulse energies of 30, 50, and 100 pJ, using pulse repetition rates ranging from 130 to 245 kHZ, and applying a target detection rate ranging from 1% to 6.5%. The measurements show homogeneous distribution of elements as can be seen in Figure 5.2B.

5.2 X-ray scattering measurements

There are two main X-ray sources: laboratory diffractometers and synchrotron facilities. Since all X-ray related work presented in this thesis uses synchrotron radiation, all discussions of X-ray experiments herein refer to measurements performed using synchrotron sources. There are two main reasons for the choice of synchrotron X-rays. First, the very high photon flux of synchrotron X-rays is essential for reliable measurement of diffuse scattering, which would require impractically long counting times on laboratory diffractometers due to their much lower signal-to-noise ratio. Second, the resolution of the PDF is dependent on the maximum measurement range in reciprocal space ($Q_{\max}$), so a high $Q_{\max}$ is critical to minimise Fourier-transform artefacts such as termination ripples. Synchrotron X-rays facility allows transmission-geometry measurements using large 2D area detectors and short sample-to-detector distances, enabling a large $Q_{\max}$.

Synchrotron X-rays are produced by accelerating electrons to near-light speed and forcing them to travel in a curved path using a magnetic field. As the electrons travel around the storage ring, they are deflected by magnetic fields produced by insertion devices (undulators or wigglers). The rapid change in direction causes the electrons to emit electromagnetic radiation due to the

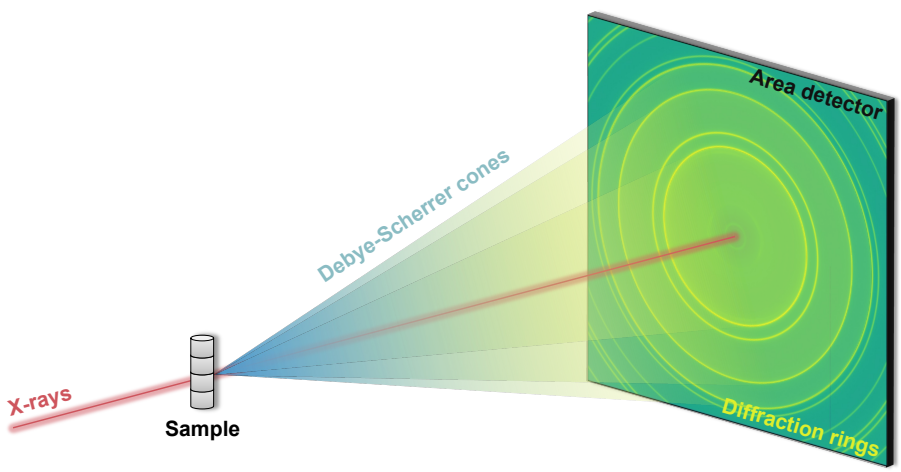

Figure 5.3: Schematic illustration of a synchrotron X-ray diffraction experiment in Debye-Scherrer (transmission) geometry.

centripetal acceleration, generating X-rays of exceptionally high intensity and collimation. The intensity and wavelength can be tailored by adjusting the energy of the electrons and the properties of the insertion devices. Additionally, the high flux of synchrotron X-rays offers a significant advantage for time-resolved measurements, enabling the capture of structural changes that occurs on millisecond to microsecond timescales.

In this thesis, X-ray total scattering and high-resolution diffraction experiments were performed at the P02.1 [79], P21.1 [80], and P21.2 [81] beamlines at the PETRA III synchrotron facility (DESY, Hamburg, Germany). Total scattering measurements at P02.1 (Paper I) were performed at a photon energy of 59.8 keV using a downstream VAREX XRD 4343CT area detector at a sample-to-detector distance of 0.301 m ($Q_{\max} = 21.04$ Å^{-1}). High-resolution diffraction experiments at P21.2 (Paper I) were performed at 82 keV, using a four-bounce channel-cut Si 111 monochromator (energy resolution of 10^{-4}) together with a multi-detector setup of four VAREX XRD 4343CT detectors, covering a large Q-range while maintaining a 2.94 m sample-to-detector distance to optimise resolution. Additional high-resolution diffraction data were collected at P21.1 (Paper IV) with a energy of 101.41 keV, using a Perkin-Elmer XRD1621 detector at a sample-to-detector distance of 1.6 m. In all experiments powder samples were contained in 1 or 1.5 mm quartz glass capillaries. Calibration was performed with NIST 660c LaB_6 or Ni powder, and background measurements were conducted for total scattering data. A schematic of a typical synchrotron X-ray diffraction experiment in transmission geometry is shown in Figure 5.3. The incident X-ray beam produces Debye-Scherrer cones upon interacting with the sample, which appear as diffraction rings on the area detector(s).

5.3 Neutron scattering measurements

The magnitude of scattering is dependent on the species of atoms. For a certain species, X-rays scatter from the electron cloud, and since the magnitude of the scattering is proportional to the scattering angle it is therefore Q-dependent. This is in contrast to neutrons, which scatter from the nucleus, and since each species has a characteristic scattering length, the magnitude of the scattering is Q-independent for any given species. This is important as the decay of the diffraction intensity is used as an indicator of atomic displacements (see Section 4.1.1.5), the Q-dependent X-rays form factor can introduce complexity and errors in the analysis. Therefore, neutron radiation is chosen as the primary probe in this thesis.

Neutrons are generally produced in two ways: at spallation sources or nuclear reactors. Spallation sources produce pulsed neutrons by bombarding a heavy metal target with accelerated proton packets (with the exception of SINQ at PSI, Switzerland), so experiments are carried out using the time-of-flight (TOF) method. Reactors produce a high flux of continuous neutrons through the process of nuclear fission, these beams are typically monochromated and used with angular dispersive diffractometers. In this section, the TOF

diffractometer GEM at the spallation source ISIS, and a constant-wavelength diffractometer at the reactor source ILL are introduced.

5.3.1 Time-of-flight neutron scattering

ISIS Neutron and Muon Source is a spallation neutron facility. The produced neutrons are slowed down to a usable energy range through moderators (typically water or liquid methane). Unlike reactor source, where neutrons are generated continuously, ISIS operates as a pulsed source, where protons are accelerated in discrete packets to bombard the target, producing many neutrons simultaneously (usually 15-20 neutrons per proton). As a result, TOF is required to determine neutron energies/wavelengths for experiments at ISIS.

According to the de Broglie relationship:

$$\lambda = \frac{h}{mv}, \tag{5.1}$$

where h is the Planck's constant, m is the mass, and v is the velocity. Insert Equation (5.1) into Bragg's law (Equation (4.8)), and in the case of first-order reflection ($n = 1$):

$$\lambda = \frac{h}{mv} = \frac{ht}{mL} = 2d \sin\theta \tag{5.2}$$

where t is the neutron flight time from the moderator to the detector and L is the distance between them. The neutron wavelength can thus be determined directly from its measured flight time, given known moderator-to-detector distance (L) at a specific neutron beamline. Since the neutron wavelength varies with its momentum, the determination of the lattice spacing d requires measuring the scattering at a fixed angle θ, the detector geometry is therefore arranged to record neutrons at well-defined scattering angles.

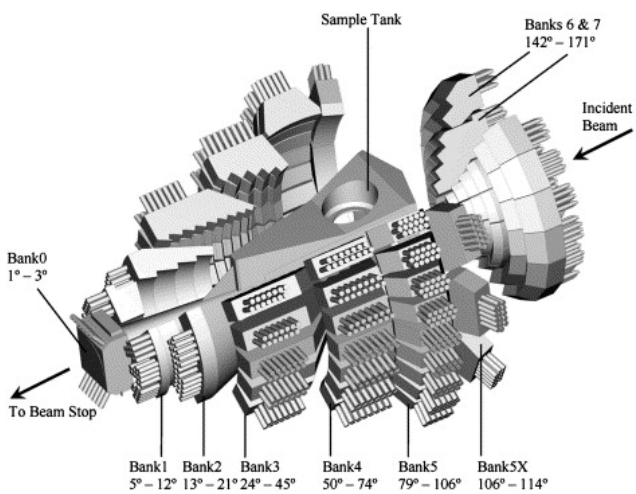

Figure 5.4: A schematic illustration of the GEM diffractometer at ISIS. *Reprinted from Ref. [82] with permission from Elsevier.*

Figure 5.4 shows a schematic illustration of the GEM diffractometer, which is positioned 17 m from the moderator. The entire instrument is evacuated to minimise neutron beam attenuation by air and to reduce background scattering. GEM [82], [83] is equipped with 7270 individual detector elements, covering a 2θ range from 1.1° to 169.3°. These detectors are arranged along the Debye-Scherrer cones, where low-angle detectors provide lower resolution but are able to access higher d-spacing, while high-angle detectors have higher resolution but are limited to lower d-spacing. These detector elements are grouped into 6 discrete banks as shown in Figure 5.4, each with an approximately constant $\Delta d/d$ resolution (so-called *resolution focused*). Consequently, this design requires an additional normalisation step as neutrons scattered from the same d-spacing will reach different detector elements with slightly different TOF. The detectors consist of ZnS/^{6}Li scintillators, which convert neutrons to photons, and photomultiplier tubes that convert photons to electric signals.

At GEM the sample tank is located beneath the floor and the samples are mounted on a long stick, which is then adjusted so that the sample is precisely positioned at the centre of the incoming neutron beam. Typically, samples are loaded into thin-walled cylindrical vanadium cans, with various lengths and diameters available to meet experimental needs. Vanadium is an ideal material for sample containers in neutron scattering experiments because it has an extremely small coherent scattering cross-section (0.0184 barns), which produces negligible Bragg peaks, in other words, it is almost "invisible" to the neutron beam. The remaining scattering is almost entirely incoherent (5.08 barns), generating a smooth and featureless background that can easily be subtracted. All standard ISIS sample environments can be mounted on GEM, including cryostats (low-temperature experiments), furnaces (high-temperature experiments), electrical measurement setups (electrical/electrochemical properties), and pressure cells (high-pressure experiments).

At the beginning of each operational cycle at ISIS, calibrations are carried out to calculate the path length between the sample and detectors. A vanadium rod with the same size as the sample can is measured and used to normalise the data. Before measuring the samples, sample container and sample environment runs are conducted and subtracted as backgrounds to remove sample-unrelated contributions for total scattering measurements. The samples are then measured, which usually takes a couple of hours depending on the scattering power of the material.

In this thesis, both a heterogeneous HfNbTaTiZr powder sample and a homogeneous HfNbTaTiZr bulk sample were measured at GEM. The powder sample was mounted in a 11 mm vanadium can and measured at room temperature, with diffraction patterns collected over five one-hour measurements, corresponding to an accumulated proton beam current of 175×5 μA to improve counting statistics. The bulk sample was measured at temperatures of 300, 150, 75, 25 and 5 K, with each temperature point accumulating an equivalent beam current of 333 μA. In both experiments, similar measurements were performed on a Nb powder reference to account for instrumental contributions.

5.3.2 Constant-wavelength neutron scattering

Another typical type of neutron scattering uses a constant-wavelength neutron beam at reactor sources. Part of the neutron data in this thesis was collected at the D4 diffractometer at Institut Laue-Langevin (ILL), France. D4 is a two-axis diffractometer; a schematic layout is shown in Figure 5.5. It uses a monochromatic neutron beam from the hot source, with available wavelengths of 0.7, 0.5 and 0.35 Å. The wavelength is selected by rotating the monochromator crystal to change the Bragg angle, using either Cu(220) or Cu(331) single crystals. The sample is then positioned inside an evacuated cylindrical bell jar. As at GEM, samples are also contained in cylindrical vanadium cans with a maximum illuminated cross-section of 20 mm (horizontal) × 50 mm (vertical). D4 is equipped with an array of nine 3He-gas 1D microstrip detectors, each covering 8° in 2θ. Because of the 7° gap between adjacent detectors, 5–6 angular positions are usually scanned to obtain a complete diffractogram with uniform counting statistics. The accessible 2θ range is 1.5° to 140°. Since the wavelength is fixed, TOF carries no energy information and therefore constant-wavelength diffraction does not require time resolution. Instead, the detectors must have a high spatial resolution in order to measure the scattering angle 2θ precisely. The microstrip detector system at D4 provides a high counting rate with good spatial resolution and excellent counting rate stability, with signal fluctuations of only 0.02% over nearly 3 days [84].

Neutron total scattering experiments of NbTaTiZr and MoNbTaW powder sample were conducted on the D4 diffractometer, using a constant wavelength

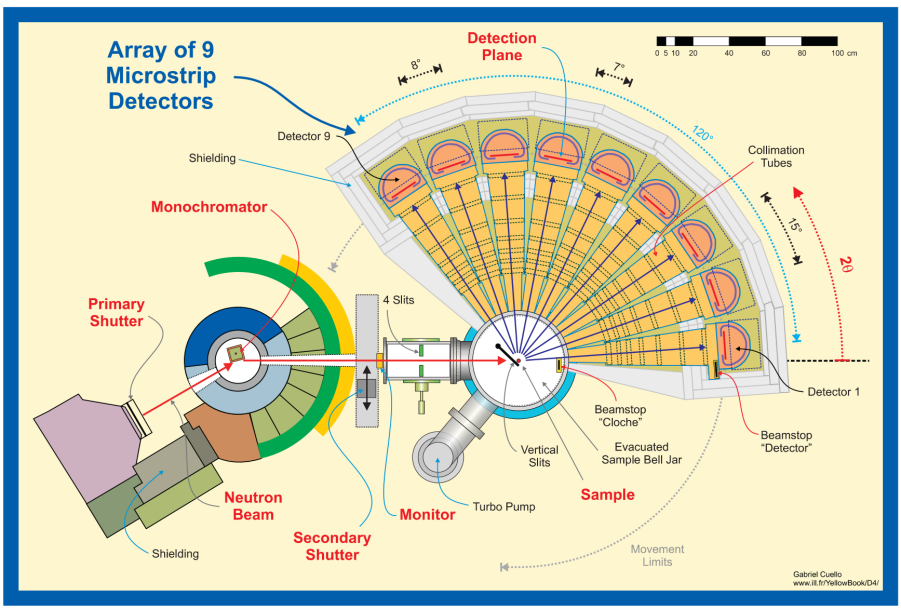

Figure 5.5: Top-view schematic of D4 diffractometer at ILL [84]. *Reproduced with permission from Springer Nature.*

of 0.496065 Å. Each sample was measured at temperatures of 300, 156, 75, 40, 20, 10, 5, 3.1 and 2 K. All samples were mounted in vanadium cans with a diameter of 4.7 mm. Identical measurements were conducted on Nb for reference.

5.4 Data analysis

5.4.1 X-ray data processing

PyFAI (Python Fast Azimuthal Integration) [85] was used for calibration using data from a reference sample LaB_6 or Nickel, and for converting the 2D images into 1D diffraction pattern. For X-ray total scattering data of the HfNbTaTiZr powder sample, the data was Fourier transformed to PDF using PDFgetX3 [86] with $Q_{\max} = 21.04$ Å^{-1}.

5.4.2 Neutron data processing

For the data obtained from GEM (HfNbTaTiZr powder and bulk), the raw scattering data were processed using the Mantid software [89], [90], which was used to merge detector signals, apply absorption corrections, and generate 1D diffraction patterns. Further processing was carried out using GudrunN software [88] to remove instrument and container backgrounds. The GudrunN software calculates an attenuation correction as part of the data reduction process to account for neutrons absorbed by atoms. Specifically, a neutron resonance occurs when the energy of an incident neutron matches with one of the discrete excited states of the compound nucleus. Each nucleus has several quantised excitation levels, and each level corresponds to a specific neutron energy. Here the resonance is expressed in wavelength according to

$$E = \frac{h^2}{2m_n\lambda^2}, \tag{5.3}$$

where h is Planck's constant, m_n is the mass of neutron and λ is the wavelength. At these resonance wavelengths, the neutron mean free path is significantly reduced, resulting in degradation of the scattering data quality. To avoid

Table 5.3: Neutron coherent scattering length b (from Ref. [87]) and resonance wavelengths (from Ref. [88]) of elements in the studied RHEAs.

Elements	Hf	Mo	Nb	Ta	Ti	W	Zr
b (fm)	7.77	6.715	7.054	6.91	-3.438	4.86	7.16
Resonance	0.273	0.083	0.048	0.138	/	0.140	0.017
wavelength	0.185	0.043	0.044	0.089	/	0.104	0.011
(Å)	/	0.034	0.029	0.076	/	0.066	/

interference from neutron resonances of the elements, the wavelength range was manually restricted to 0.3–3.55 Å. The neutron resonance wavelengths and coherent scattering length of the elements in the materials are provided in Table 5.3.

The processed data were subsequently Fourier transformed to real-space PDFs with $Q_{\max} = 34$ (HfNbTaTiZr powder) and 25 (HfNbTaTiZr bulk) Å^{-1}. This $Q_{\max}$ was chosen for a sufficient resolution without including too much noise from high Q data. It should be noted that the term PDF in this thesis refers to $G(r) = 4\pi r[\rho(r) - \rho_0]$; a detailed discussion of the nomenclature can be found in [60]. Since the PDF peak width is of most importance in this analysis, the Lorch function was not applied to avoid artificial broadening and additional errors.

Data obtained from D4 (NbTaTiZr and MoNbTaW powder) were processed using the onsite programme to produce 1D diffraction patterns. To produce PDFs, further processing was carried out using the PDFgetN3 software [91], which first removed instrument and container background and then subsequently Fourier transformed to real-space PDFs with $Q_{\max} = 23.5$ Å^{-1}.

5.4.3 Rietveld refinement

Rietveld refinements of the 1D diffraction patterns were carried out using TOPAS [92] for the GEM data (bank 5) and GSAS-II [93] for the D4, P21.2, and P02.1 data. Both softwares use the Rietveld method [94], which is a well-established and widely acknowledged method in the field of crystallography. It uses the least-squares method adjusted to the crystal structure model to closely match the observed diffraction pattern, thereby enabling the structural refinement of diffraction data.

The diffraction data (background, arbitrary scaling factor, and instrument parameters) of the standard sample/calibrant (LaB_6 or Ni) is refined while the phase-related parameters (lattice parameters, site occupancies, atomic positions and atomic displacement parameters etc.) remain fixed. As the standards have known lattice parameters and are confirmed to have no strain or size-related broadening, it is possible to isolate the instrumental contribution. An instrument parameter file is generated to be used in refinements of samples.

In the subsequent refinement process of samples, the instrument parameters remained fixed while sample-related parameters are refined. Here, lattice parameter a, isotropic atomic displacements parameter U_{iso}, and microstrain were refined. U_{iso} was constrained to be the same for all atoms within the bcc structure (space group $Im\bar{3}m$). The unit cell's site occupancy was based on the alloy's average composition from EDS (see Table 5.1 and 5.2). Microstrain was refined to obtain good fits, though the resulting values are not considered as physical strains. Significant broadening of the diffraction peaks of the powder samples were observed, and the available parameters to describe this are crystalline size and microstrain. However, a significant part of the broadening is expected to be related to the continuous variation of the composition (lattice parameter) across the dendrites and interdendritic regions since there are no sharp phase boundaries (Figure 5.1). The software does not allow the use of a

"lattice parameter distribution" to capture this, so the microstrain parameter was used as a dummy parameter to capture the peak broadening, including the lattice parameter distribution. Adding size broadening did not improve the fit significantly, but lead to unstable fits since it has a very high correlation with the microstrain parameter, therefore it was not used. With a and U_{iso} extracted, LLDs were able to be calculated according to Equation 3.1

$$\varepsilon_{\mathrm{s}} = \frac{\sqrt{U_{\mathrm{iso}} - U_{\mathrm{thermal}}}}{\frac{\sqrt{3}}{4}a}, \tag{5.4}$$

and the method of determining the thermal component of the displacement parameter U_{thermal} was discussed in Section 4.2.

5.4.4 Small-box analysis

Small-box analysis of the PDFs was performed in the PDFgui software [61], or in the DiffPy-CMI framework [62], with a fitting range of 0.5-20 Å. The refined parameters included the lattice parameter a, the correlated motion factor δ_2 (more appropriate for the case of low temperature), the scale factor, the isotropic atomic displacement parameter U_{iso} and Q_{broad}. A constrain $u_{11} = u_{22} = u_{33}$ was applied, which is a reasonable assumption for metallic systems. Q_{damp} was first fitted from a reference at room temperature and then fixed for subsequent fits. According to Equation 5.4, LLDs were calculated.

5.4.5 Large-box analysis

RMCProfile [95], [96] is based on the reverse Monte Carlo method. The analysis begins by constructing an atomic configuration consisting of a large supercell containing thousands of atoms, arranged in a periodic order according to the given crystal structure, with all atoms initially positioned at their ideal lattice sites without any displacements. This configuration is then fitted against experimental data (reciprocal-space diffraction patterns and real-space PDFs can be fitted simultaneously in RMCProfile) by allowing certain atoms to move randomly, and the quality of the fit is quantified by the goodness-of-fit parameter χ^2, defined as:

$$\chi^2 = \sum_{i}^{\text{datasets}} w_i \sum_{j}^{\text{points}} \left(\frac{y_{ij}^{\mathrm{exp}} - y_{ij}^{\mathrm{calc}}}{\sigma_{ij}} \right)^2, \tag{5.5}$$

where w_i is the weighting factor of dataset i, y_{ij}^{exp} and y_{ij}^{calc} are the experimental and calculated values of data point j in dataset i, respectively, and σ_{ij} is the experimental uncertainty. An iterative process is run, where atomic moves that decrease χ^2 are always accepted, while those that increase χ^2 by $\Delta\chi^2$ are also accepted with a probability $P = \min[1, \exp(-\Delta\chi^2/2)]$, making sure that the system will not get stuck in local minima. Moreover, moves that contradict constraints, e.g. distance window, bond valence sum, bond angle etc., are rejected no matter if it increases or decreases $\Delta\chi^2$. Following this

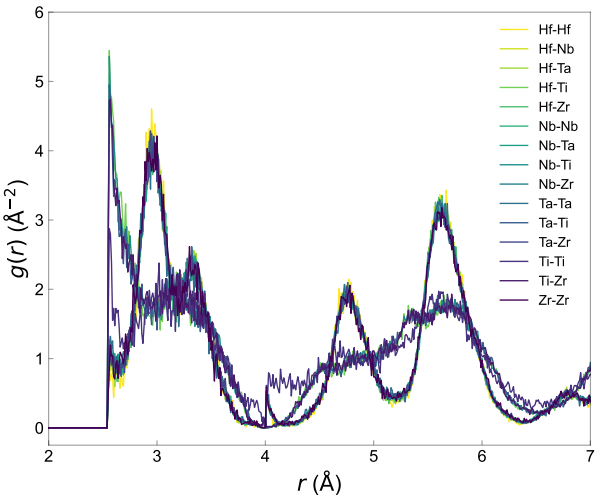

Figure 5.6: Partial PDFs of HfNbTaTiZr from RMCProfile. All partials containing Ti exhibit physically unrealistic distributions.

iterative process, the number of accepted atomic moves increases and the fit to the experimental data becomes better.

RMCProfile was first run using a "coloured" configuration for the HfNbTaTiZr bulk sample, meaning that the configuration contains all five constituent elements. However, this method generated problematic distributions in the partial PDFs. As shown in Figure 5.6, the Ti-related peaks are broadened and distributed as local maxima at low r region. Because of the negative scattering length of Ti (see Table 5.3), the software tries to move the Ti atoms to compensate for intensity variations in the pattern, which results in unrealistic peak shapes in the partial PDFs [97]. Therefore in the following analysis, a "grey-atom" model was used in which all atomic species were treated as a single representative atom.

For the five temperatures, each dataset was initially fitted in RMCProfile for 10,800,000 iterations. However, some fittings were interrupted due to computer issues and did not reach full iterations, this explains the different χ^2 values in Figure 5.7A. Nevertheless, all fits appear good and the extracted results should be reliable. The atomic positions from both the initial configuration (denoted as superscript i) and the final calculated configuration (denoted as superscript c) were extracted and used to calculate the atomic displacements, defined as:

$$r = \sqrt{(r_x^{\mathrm{c}} - r_x^{\mathrm{i}})^2 + (r_y^{\mathrm{c}} - r_y^{\mathrm{i}})^2 + (r_z^{\mathrm{c}} - r_z^{\mathrm{i}})^2}, \tag{5.6}$$

where r_x is the coordinates at x axis and so on. The distribution of the calculated atomic displacements extracted from RMCProfile at each temperature are shown in Figure 5.7B–F. A general broadening of the distribution with increasing temperature is observed, indicating that atoms become more displaced from their ideal lattice sites at higher temperatures. The histograms are fitted

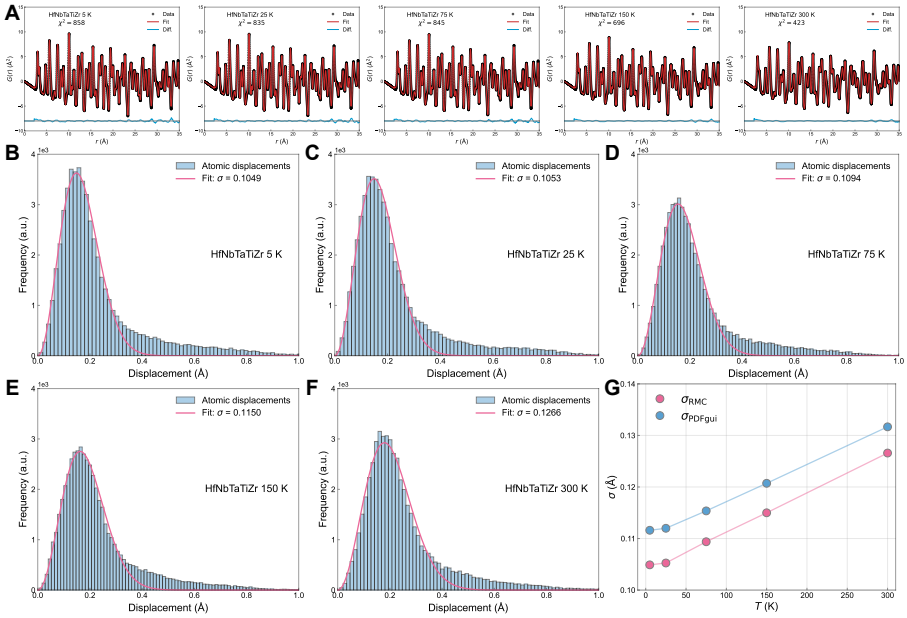

Figure 5.7: **(A)** RMC fitting of the PDFs of HfNbTaTiZr at various temperatures. Atomic displacements distribution of HfNbTaTiZr at **(B)** 5 K, **(C)** 25 K, **(D)** 75 K, **(E)** 150 K, **(F)** 300 K obtained from RMCProfile, fitted with a shell-corrected Gaussian distribution. **(G)** Atomic displacements σ obtained from RMC compared with those from PDFgui as a function of temperature.

using a Gaussian function with a shell correction applied to account for the increasing volume of spherical shells at larger sampling radii, described by:

$$A \exp\left(-\frac{(\mu - r)^2}{2\sigma^2}\right) 4\pi r^2, \tag{5.7}$$

where A is a scaling factor, μ is the mean of the distribution, r is the displacement defined in Equation (5.6), σ is the standard deviation, and $4\pi r^2$ stands for the geometric shell correction. The fitted value of σ is used to represent the total atomic displacements and plotted in Figure 5.7G, because RMC gives instantaneous snapshots that include both static and thermal contributions. Note that there are some atoms with high displacements falling outside the fit, which may be attributed to artefacts in the model arising from non-optimised processing parameters.

The results from RMCProfile are compared with those obtained from small-box analysis, where $\sigma_{\mathrm{PDFgui}} = \sqrt{U_{\mathrm{iso}}}$ based on the discussion in Section 4.1.1.5. Both methods show a consistent increase with temperature and the displacement values fall within a similar range, indicating a good agreement between the two methods. However, the tails observed in the distributions shown in Figure 5.7B–F could introduce additional uncertainty. For this reason, small-box analysis was adopted for quantifying LLDs and is further discussed

in the next chapter.

Chapter 6

Summary of results

6.1 Separation of thermal components

In this section, the results obtained from the four different methods for determining the thermal displacements, as introduced in Chapter 4, are presented and compared. These methods provide alternative approaches for estimating U_{thermal}, with the choice of method depending on availability of specific experimental measurements or computational resources.

6.1.1 Thermal displacements from rule-of-mixture

The current reported experimental methodology for separating the thermal component involves conducting temperature-dependent scattering experiments at cryogenic temperatures [34], [52], [53]. However, conducting in situ scattering experiments at cryogenic temperatures is not always feasible, such as when comparing multiple alloys, because these experiments are time-consuming. In such cases, approximate estimations of the thermal contribution are required. This section introduces estimating the thermal component using rule-of-mixtures (ROM).

According to Equation (4.22) and (4.23), apart from the elemental concentrations c_i, two quantities need to be determined: the Debye-Waller B-factor of element i and the temperature T at which the B-factors are calculated. The magnitude of thermal vibrations is a function of the thermal energy and the elastic constants of the material, which, in turn, are related to the melting temperature. Materials measured at the same temperature generally do not have the same magnitude of thermal displacements as their masses and force constants are different. For a meaningful comparison across materials, the B_i^T values should therefore be evaluated at the same relative temperature with respect to their melting points, i.e. at a uniform homologous temperature $\tau = T/T_m$, where T_m is the melting temperature. Using homologous temperature ensures that thermal displacements are calculated under near-equivalent thermodynamic conditions. To determine the homologous temperature, the melting temperature of the alloy, $T_{\text{m},a}$, must be known. This is often not

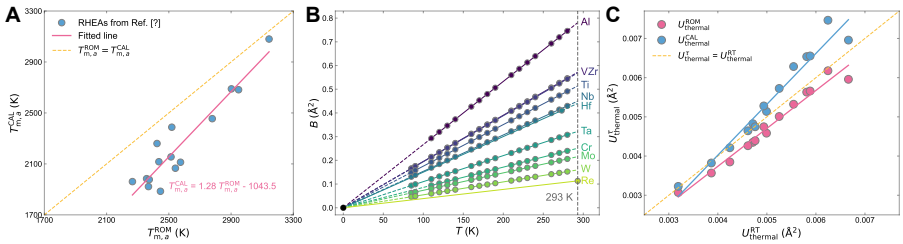

Figure 6.1: (**A**) The fitted linear relationship between $T^{\mathrm{ROM}}_{\mathrm{m},a}$ and $T^{\mathrm{CAL}}_{\mathrm{m},a}$. The blue points are the alloys investigated in Ref. [98] involving the same elements as in Ref. [26]. (**B**) Linear fit of B-factors. Values denoted as circle are derived from Ref. [99], [100], [101]. Note here that the data missing in the low temperature region is deemed less critical for this analysis, as the focus is primarily on data around room temperature. (**C**) Comparison between different methods of evaluating thermal components U_{thermal} from various RHEAs at room temperature. The solid lines are linear fits for respective methods. *This figure is reproduced from Ref. [102], licensed under a Creative Commons Attribution 4.0 International License. The colours of the symbols have been remade.*

available for RHEAs and must also be estimated from the melting points of the constituent elements. Accordingly, two methods are proposed to calculate this temperature:

- ROM method: This method applies ROM to calculate the melting temperature of the alloy ($T^{\mathrm{ROM}}_{\mathrm{m},a}$).

- CALPHAD corrected method: This method corrects the $T^{\mathrm{ROM}}_{\mathrm{m},a}$ by performing a first-order correction based on CALPHAD (CALculation of PHAse Diagrams) calculations, as demonstrated by Senkov et al. [98].

The correction is shown in Figure 6.1A. Further elaboration on these methods, including their mathematical expression, is provided in Paper I.

The other term, Debye-Waller B-factor of element i, is derived from the linear inter- and extrapolation of the values reported in Ref. [99], [100], [101], as shown in Figure 6.1B. More detailed calculation results can be found in the Supplementary Material of Paper I.

With both temperature and B-factor determined, the subsequent thermal components of the displacement parameters U^{T}_{thermal} can be calculated using Equation (4.22). This yields two values, $U^{\mathrm{ROM}}_{\mathrm{thermal}}$ and $U^{\mathrm{CAL}}_{\mathrm{thermal}}$, corresponding to the two different methods used to determine the homologous temperature (τ). Additionally, $U^{\mathrm{RT}}_{\mathrm{thermal}}$ can be calculated using room-temperature B-values for all elements for comparison. Detailed calculation results can be found in the Supplementary Material of Paper I. Figure 6.1C shows a comparison of the different approaches (at room temperature) where the overall differences are minor despite increasing discrepancies observed at high U_{thermal} values.

Different assumptions were made for the separation of thermal contributions of atomic displacements. The estimations presented here provide a readily accessible and practical methodology for isolating static displacements. This is promising for future studies, as it suggests that U_{iso}-based analysis without variable-temperature (i.e. cryogenic) measurements offers a sufficiently accurate way to measure the thermal components and, subsequently, the LLDs.

6.1.2 Thermal displacements from VDOS

The thermal displacements of a HfNbTaTiZr RHEA from the VDOS were obtained through MD simulations following the method described in Section 4.2.2. The simulated VDOS is shown in Figure 6.2A, with the contribution of each constituent element shown separately. The accuracy of the calculated VDOS is assessed by comparing the specific heat obtained from the VDOS with the experimental measurements, where the specific heat from the VDOS is calculated using the equation:

$$C_{\mathrm{v}}^{\mathrm{VDOS}} = 3R \sum_i c_i \int_0^\infty x^2 \frac{e^x}{(e^x-1)^2} g_i(f)\, \mathrm{d}f, \tag{6.1}$$

with

$$x = \frac{hf}{k_{\mathrm{B}}T}, \tag{6.2}$$

where $g_i(f)$ is the partial VDOS of element i, f is the vibrational frequency, c_i is the concentration, R is the gas constant, h is the Planck constant, and k_{B} is the Boltzmann constant. The calculated specific heat $C_{\mathrm{v}}^{\mathrm{VDOS}}$ at constant volume is corrected to make it comparable with measurements performed under constant pressure, according to:

$$C_{\mathrm{p}}^{\mathrm{VDOS}} = C_{\mathrm{v}}^{\mathrm{VDOS}} + \alpha_{\mathrm{v}}^2 B V_{\mathrm{m}} T, \tag{6.3}$$

where α_{v} is the volumetric thermal expansion coefficient (2.11 $\times 10^{-5}$ K^{-1} at 300 K [103]), B is the bulk modulus (134.6 GPa at 300 K [21]), V_{m} is the

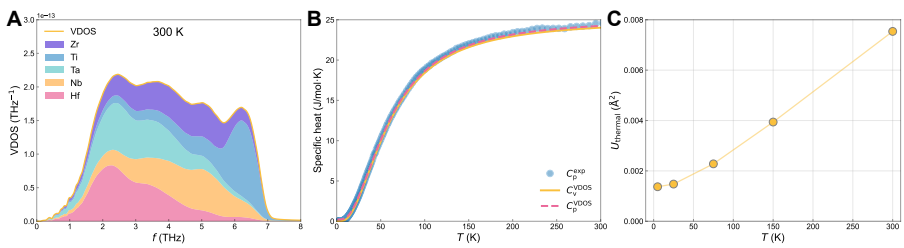

Figure 6.2: (**A**) Element-resolved partial vibrational density of states (VDOS) of HfNbTaTiZr simulated by molecular dynamics at 300 K. (**B**) Specific heat of HfNbTaTiZr from experimental measurements ($C_{\mathrm{p}}^{\mathrm{exp}}$), compared with values calculated from the VDOS ($C_{\mathrm{v}}^{\mathrm{VDOS}}$) and those corrected from the VDOS ($C_{\mathrm{p}}^{\mathrm{VDOS}}$). (**C**) Thermal displacement parameters U_{thermal} calculated from VDOS.

molar volume, and T is the absolute temperature. An upper-limit calculation using these parameters at room temperature gives a difference of less than 1% between $C_{\mathrm{v}}^{\mathrm{VDOS}}$ and $C_{\mathrm{p}}^{\mathrm{VDOS}}$, indicating that thermal expansion has a negligible effect. The calculated $C_{\mathrm{p}}^{\mathrm{VDOS}}$ align well with experimental values, as shown in Figure 6.2B, confirming the reliability of the simulated VDOS.

Using the methodology described in Section 4.2.2, the thermal displacement parameters are then calculated at the temperatures corresponding to the neutron scattering measurements (5, 25, 75, 150 and 300 K) and are shown in Figure 6.2C.

Among the methods for determining thermal components, this approach is the only element-resolved method and thus will be one of the most accurate.

6.1.3 Thermal displacements from specific heat

In the absence of VDOS information, a commonly used alternative for estimating thermal contribution is the Debye model, as described in Section 4.2.3. As shown in Figure 6.3B, the Debye model reproduces the specific heat data reasonably well, yielding a fitted Debye temperature of 233 K, which is then used to calculate the corresponding VDOS and thermal displacement parameter as shown in Figure 6.3A and C, respectively. Despite the good agreement with the specific heat data, the Debye VDOS differs from the MD-simulated VDOS, because the Debye model is a rather crude approximation of the phonon spectrum. However, specific heat depends on the integration over all phonon

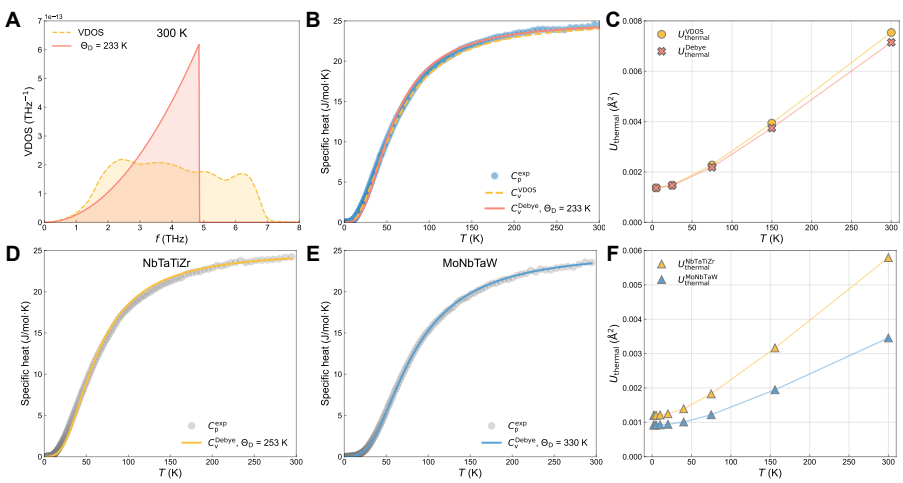

Figure 6.3: (**A**) Calculated density of states of HfNbTaTiZr from the Debye model compared with VDOS. (**B**) Debye model fit of specific heat to the measurements for HfNbTaTiZr compared with $C_{\mathrm{v}}^{\mathrm{VDOS}}$. (**C**) Thermal displacement parameters U_{thermal} calculated from the Debye model, compared with those calculated from VDOS. Specific heat measurements with Debye fit for (**D**) NbTaTiZr and (**E**) MoNbTaW. (**F**) The thermal displacement parameter U_{thermal} calculated using the Debye model for NbTaTiZr and MoNbTaW.

modes, making it relatively insensitive to spectral features. Despite this, the calculated thermal displacement parameters are very close to those obtained from the VDOS, indicating that the Debye model can be used as a practical approximation for estimating the thermal component.

The Debye approximation is also applied to NbTaTiZr and MoNbTaW, where a Debye temperature of 253 K and 330 K is obtained from fitting the specific heat data as shown in Figure 6.3D and E, respectively. It is worth noting that MoNbTaW has a higher Debye temperature despite its larger average atomic mass, which is likely attributed to its stiffer lattice, consistent with the significantly higher elastic modulus expected for this alloy compared to NbTaTiZr, as both Mo and W have much higher elastic moduli than Ti and Zr.

This summarises the different approaches for calculating and separating the thermal components. The rule-of-mixture offers an alternative when variable-temperature experiments are unavailable. Calculating thermal displacements from VDOS remains the most reliable method as it directly reflects the vibrational modes of the alloy. Specific heat measurements combined with Debye approximation provide an accessible and computationally efficient alternative that can also capture the thermal component with reasonable accuracy.

6.2 Quantification of LLDs in RHEAs

By estimating the thermal components using the methods presented in Section 6.1.1, it is possible to quantify LLDs for a range of alloys. Here, this approach is applied to quantify LLDs at room temperature in a series of RHEAs that Tong et al. reported in Ref. [26]. Furthermore, one prototype material (gas atomised equiatomic HfNbTaTiZr) was examined through total scattering data. Results indicate pronounced LLDs in the analysed bcc RHEAs, and confirm the consistency and reliability of the scattering-based techniques in probing LLDs by showing an agreement on the outcomes.

6.2.1 LLDs of RHEAs from literature

According to Equation 3.1 and the discussion in Section 4.1.1.5, U_{iso}, U_{thermal}, and a are required to calculate the values of LLDs (ε_{s}). Using the U_{iso} and a reported in Ref. [26], along with the calculated thermal components U_{thermal} obtained in Section 6.1.1, LLDs of these RHEAs are calculated and listed in Table 6.1. The reason for choosing $U_{\mathrm{thermal}}^{\mathrm{CAL}}$ is because it provides the most conservative estimation of the static contributions, i.e., the smallest LLDs.

The results presented in Table 6.1 show that there appears to be a correlation between the chemical composition and LLDs. Notably, the first three RHEAs, all of which contain Zr, exhibit significantly large LLD values (around 10%). This differs from the other RHEAs, where the average ε_{s} value is around $5.85 \pm 1.0\%$, with small variations. It is observed that the addition or removal of Hf and Zr is expected to significantly affect LLDs, which might be due to the extensive charge transfer and associated change in effective atomic size [26], [35], [36].

Table 6.1: Values of LLDs (ε_s), displacement parameters (U_{iso}), lattice parameters (a), thermal ($U^{CAL}_{thermal}$) and static (U_{static}) components of the displacements for RHEAs studied in Ref. [26].

Composition	ε_s (%)	U_{iso}† (Å^2)	$U^{CAL}_{thermal}$* (Å^2)	U_{static}* (Å^2)	a† (Å)
HfNbTaTiZr	10.18	0.0291	0.0065	0.0226	3.4088
HfNbTiZr	9.91	0.0292	0.0075	0.0217	3.4359
NbTiVZr	10.61	0.0302	0.0070	0.0232	3.3181
MoNbReTaTiVW	4.66	0.0083	0.0042	0.0041	3.1678
MoNbReTaVW	4.54	0.0077	0.0038	0.0039	3.1653
MoNbTaTiVW	5.50	0.0106	0.0048	0.0058	3.1911
MoNbReTaW	4.08	0.0064	0.0032	0.0032	3.1901
MoNbTaTiV	6.85	0.0148	0.0057	0.0091	3.2119
NbReTaTiV	6.67	0.0136	0.0051	0.0085	3.1865
MoNbTaV	6.18	0.0126	0.0053	0.0073	3.1998
MoNbTiV	6.53	0.0144	0.0063	0.0081	3.1846
NbReTaV	5.80	0.0110	0.0046	0.0064	3.1750
NbTaTiV	6.57	0.0150	0.0066	0.0084	3.2319
NbTaVW	6.39	0.0126	0.0047	0.0079	3.2043
Nb	0	0.0060	-	0	3.2980

† From Ref. [26].
* From Ref. [102].

The magnitudes of the static and thermal components of the off-site displacement parameter in RHEAs are visually illustrated in Figure 6.4. Notably, the static components are shown to be of comparable level to (or even surpassing) that of the thermal components. This is in contrast to the case of fcc-structured HEAs, where the thermal displacements are larger than the static displacements [34], indicating the pronounced LLDs in bcc-structured RHEAs.

6.2.2 LLDs of a HfNbTaTiZr RHEA

As in the preceding section, LLDs of the HfNbTaTiZr RHEA were quantified using the lattice parameter a and displacement parameter U_{iso} (both obtained from the scattering data) and the thermal component $U_{thermal} = 0.0065$ Å^2 (determined in Section 6.1.1). The results are summarised in Table 6.2. Com-

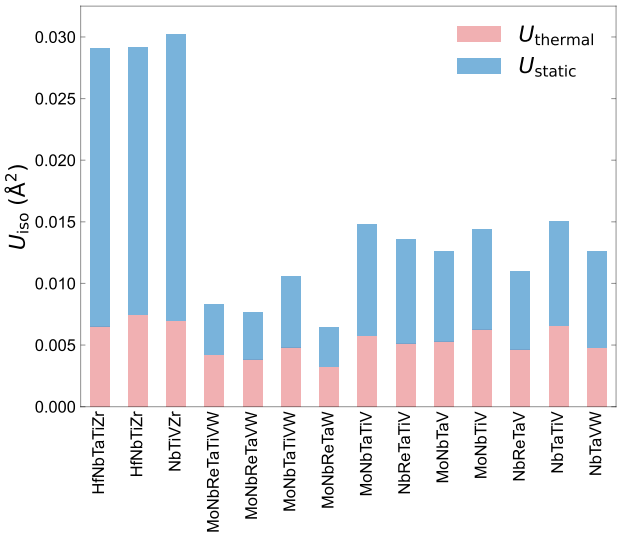

Figure 6.4: Static (U_{static}) and thermal (U_{thermal}) component of the off-site displacement parameter (U_{iso}) extracted from several RHEAs [26]. U_{thermal} is calculated in section 6.1.1, and U_{iso} is determined experimentally by Tong et al. [26] from diffraction data. The relatively larger magnitude of U_{static} than U_{thermal} indicates that LLDs in bcc-structured RHEAs are pronounced. *This figure is reproduced from Ref. [102], licensed under a Creative Commons Attribution 4.0 International License. The legend has been modified.*

parison across different analytical methods (diffraction and PDF) as well as radiation type (X-ray and neutron), shows notable consistency in LLDs. Such agreement indicates the reliability and robustness of these techniques and sources in accurately quantifying LLDs. It is noted that the LLD value derived from X-ray diffraction refinement is 6.53%, which is significantly smaller than

Table 6.2: Comparison of lattice parameters (a), off-site displacement parameters (U_{iso}), and LLD (ε_{s}) for the HfNbTaTiZr RHEA from reciprocal-space (diffraction) and real-space (PDF) analysis of X-ray and neutron data. *This table is reproduced from Ref. [102], licensed under a Creative Commons Attribution 4.0 International License. No changes were made.*

	X-ray		**Neutron**
	Diffraction	PDF	PDF
a (Å)	3.4019(1)	3.4010(8)	3.4041(6)
U_{iso} (Å^2)	0.0158(2)	0.0197(6)	0.0168(4)
ε_{s} (%)	6.53	7.76	7.16

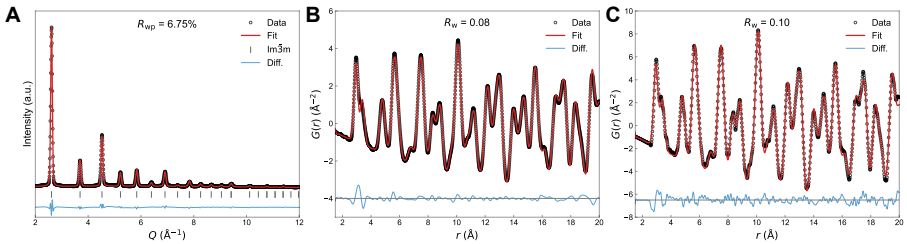

Figure 6.5: (**A**) Rietveld refinement of a X-ray diffractogram of HfNbTaTiZr at room temperature. (**B**) The X-ray and (**C**) neutron PDF with small-box fitting of HfNbTaTiZr at room temperature. *This figure is reproduced from Ref. [102], licensed under a Creative Commons Attribution 4.0 International License. The colours of the symbols and the legend have been remade.*

the value obtained from U_{iso} reported by Tong et al. [26] (10.18%, see Table 6.1). Without comprehensive data for other alloys, it is uncertain whether this difference represents a systematic variation across different RHEAs, or is specific to the HfNbTaTiZr RHEA. Further investigations into a wider range of RHEAs are required to clarify this discrepancy.

Rietveld refinement of the X-ray diffractogram of HfNbTaTiZr is shown in Figure 6.5A, where a significant decay in intensity with increasing Q is observed, due to the combined effects of LLDs, thermal vibrations, and X-ray form factor as previously discussed in Section 4.1.1.5. Furthermore, the PDF fitting shown in Figure 6.5B and C exhibit overall good agreement between the experimental data and the model.

This demonstrates the quantification of LLDs for a range of RHEAs from Ref. [26] and results show that LLDs are pronounced within bcc-structured RHEAs compared to their fcc-structured counterparts. Further analysis of a HfNbTaTiZr RHEA shows a good agreement between real-space (PDF) and reciprocal-space (diffraction) results of X-ray scattering data. Additionally, consistent results between neutron and X-ray PDF analyses indicate that the radiation type has a negligible impact.

6.3 The effects of segregation on the determination of LLDs

Quantification of LLDs using single-phase small-box modelling assumes that the studied material is homogeneous, i.e., free of heterogeneity such as chemical segregation, microstrain, or nonuniform crystallite size. However, this does not always reflect reality, as demonstrated by the dendritic microstructures observed in the HfNbTaTiZr powder sample (Figure 5.1). Similar microstructures have also been observed in various as-cast RHEAs as shown in Figure 2.3 and in literature [17], [104]. These dendritic microstructures arise from the alloys' compositional complexity and the varying melting temperatures of their constituent elements [105]. This observation raises a critical question about

the potential impact of chemical segregation on the validity of the single-phase small-box analysis. To address this question, a comprehensive simulation study was conducted. Theoretical PDFs were generated to mimic the segregated microstructures of the HfNbTaTiZr RHEA and subsequently fitted using a single-phase model. This approach was further extended to a wider range of RHEAs, aiming for a broader understanding of how chemical segregation may affect the accuracy of LLD determination. The simulation and fitting were performed using the DiffPy-CMI modeling framework [62].

6.3.1 Quantifying LLD errors in HfNbTaTiZr

A segregated microstructure is characterised by continuous modulations in its chemical composition. For simplicity, it can be approximated as a two-phase system comprising dendrites (D) and interdendritic regions (ID). Each phase has a distinct chemical composition and therefore a different lattice parameter. Following the methodology proposed by Sławiński [106], the overall PDF of such a multiphase system can be mathematically expressed as a weighted sum of the PDFs of the individual phases:

$$G(r) = \sum_p \frac{x_p \bar{b}_p^2}{\sum_p x_p \bar{b}_p^2} G_p(r), \tag{6.4}$$

where x_p is the molar fraction, $\bar{b}_p$ is the average neutron scattering length, and $G_p(r)$ is the PDF of phase p. $\bar{b}_p$ can be calculated based on the chemical composition of dendrites and interdendritic regions ($\bar{b}_p = \sum_i c_{i,p} b_{i,p}$), as shown in Table 6.3. When the difference in lattice parameters between the two "phases" is small, volume fractions may be used as a substitute for molar fractions.

To simulate two-phase PDFs, parameters such as lattice parameters and volume fractions are required. These parameters were obtained from the Rietveld refinement of high-resolution synchrotron X-ray diffraction data, as shown in Figure 6.6A. The segregation can be clearly seen from the slightly asymmetric 110 peaks in Figure 6.6B. The refinement yields lattice parameters of $a_{\mathrm{D}} = 3.3938(1)$ Å for the dendrites and $a_{\mathrm{ID}} = 3.4129(2)$ Å for the interdendritic regions, and a volume fraction of $V_{\mathrm{F}} = 0.47(1)$.

A theoretical two-phase PDF was generated using the lattice parameters for both phases (a_{ID} and a_{D}) and an identical U_{iso} value (0.0168 Å^2 from the neutron PDF data). The resulting two-phase PDF was then compared with a single-phase PDF ($a = 3.4041$ Å, U_{iso} =0.0168 Å^2) as shown in Figure

Table 6.3: Calculated average values of coherent neutron scattering lengths ($\bar{b}$) for dendrites and interdendritic regions based on their chemical composition and Table 5.3.

	Dendrites	Interdendritic regions
$\bar{b}$ (fm)	5.24	4.31

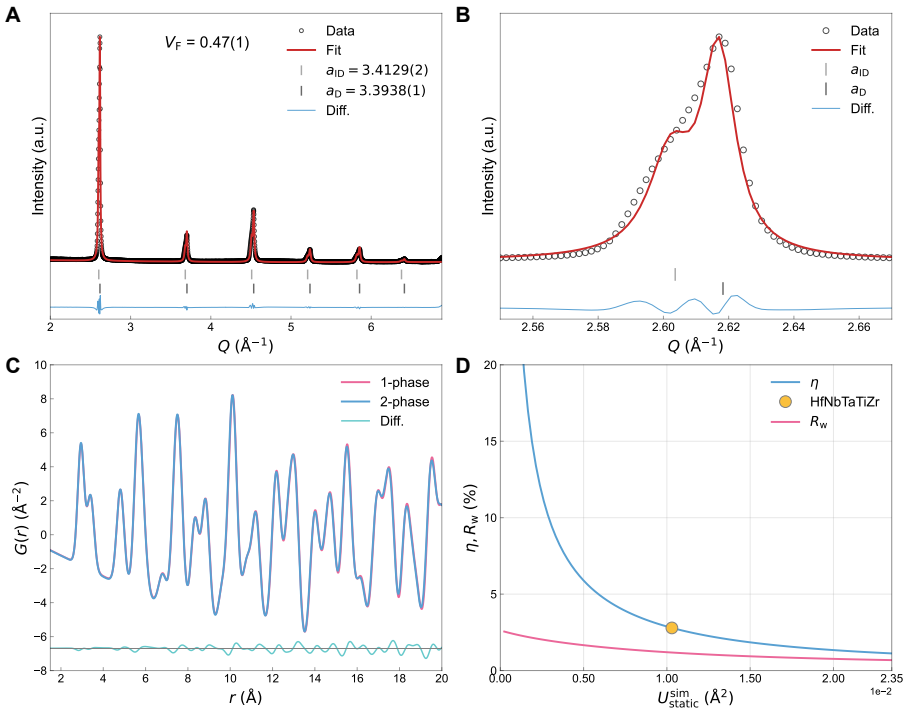

Figure 6.6: (**A**) Two-phase Rietveld refinement of the high-resolution X-ray diffractogram of HfNbTaTiZr. (**B**) Enlarged view of the 110 reflection showing asymmetric peak due to chemical segregation. (**C**) Comparison of simulated PDFs for the HfNbTaTiZr alloy in homogeneous (1-phase) and segregated (2-phase) microstructures. (**D**) Error (η) distribution of LLDs from single-phase PDF analysis of simulated PDFs, as a function of the LLDs magnitude ($U^{\text{sim}}_{\text{static}}$). The yellow circle denotes the HfNbTaTiZr alloy from our experimental data. R_{w} values indicate the quality of the fits. *This figure is reproduced from Ref. [102], licensed under a Creative Commons Attribution 4.0 International License. The colours of the symbols and the legend have been remade.*

6.6C, where only minor deviations at higher r values are observed, indicating that chemical segregation has a negligible impact on the PDF for the studied HfNbTaTiZr. To further explore the effect of segregation on determining LLDs, a series of two-phase PDFs with varying U_{iso} values were simulated and fitted using a single-phase model. The relative error of LLDs between the fitted and the simulated data, η, is defined as

$$\eta = \frac{|\varepsilon_{\text{fit}} - \varepsilon_{\text{sim}}|}{\varepsilon_{\text{sim}}}, \tag{6.5}$$

where ε_{fit} is the LLD calculated from the parameters obtained by fitting the generated two-phase PDF with a single-phase model, and ε_{sim} is the LLD calculated using the parameters used to generate the two-phase PDF (more details in Paper I). The results are presented in Figure 6.6D, where an inverse

correlation between $U^{\text{sim}}_{\text{static}}$ (the simulated static component) and η is seen. A rapid increase in error is observed at lower $U^{\text{sim}}_{\text{static}}$ values, where care must be taken. However, for the studied HfNbTaTiZr RHEA, depicted as a yellow circle in Figure 6.6D, the error is around 3%, which is acceptable and should not be a problem on the determination of its LLD. On the other hand, the R_{w} values which represent the fitting quality do not show significant increase at decreasing $U^{\text{sim}}_{\text{static}}$, probably due to the small lattice parameter difference between the two phases (3.3938 and 3.4129 Å, a difference of only 0.56%).

6.3.2 Quantifying LLD errors in RHEAs

While the analysis indicates that segregation only has a minimal impact on the determination of LLDs in the HfNbTaTiZr, this conclusion may be specific to this system. To develop a broader understanding of how segregation influences LLD errors across different alloys, a comprehensive simulation study was carried out for generic bcc-structured HEAs. The effect of differences in scattering lengths between dendritic and interdendritic regions on the accuracy of LLD quantification was also investigated.

Similar simulations and fittings were performed as in the preceding section. First, the impact of variation in lattice parameters and molar fractions on the accuracy of LLDs measurements was investigated. A maximum difference in lattice parameters of 3% between the two phases ($\Delta a = |a_2 - a_1|/a_1$) was applied, based on values reported in the literature (0.6–3.3%, see Paper II). For each Δa, the static displacement parameter $U^{\text{sim}}_{\text{static}}$ was varied from 0 to 0.025 Å^2. Finally, the molar fraction of one phase X_{ID} was assigned four values, 0.125, 0.25, 0.375 and 0.5.

Figure 6.7A shows the resulting two-phase PDFs corresponding to the extreme cases with $X_{\text{ID}} = 0.5$. In scenarios where significant LLDs are present (i.e., at high $U^{\text{sim}}_{\text{static}}$ values), the effect of segregation on the PDF is relatively minor, as seen by the similarity between the teal and yellow curves. In contrast, when LLDs are absent ($U^{\text{sim}}_{\text{static}} = 0$), segregation has a much more pronounced effect, leading to noticeable discrepancies in the PDFs (as illustrated by the

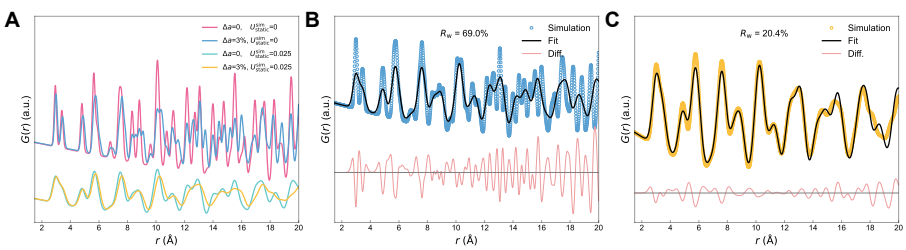

Figure 6.7: (**A**) Four extreme cases of simulated composite PDFs with $X_{\text{ID}} = 0.5$. Single-phase fits to the PDFs corresponding to (**B**) $\Delta a = 3\%/U^{\text{sim}}_{\text{static}} = 0$, and (**C**) $\Delta a = 3\%/U^{\text{sim}}_{\text{static}} = 0.025$. R_{w} values indicate the quality of the fits. *This figure is reproduced from Ref. [107], licensed under the Creative Commons CC BY license.*

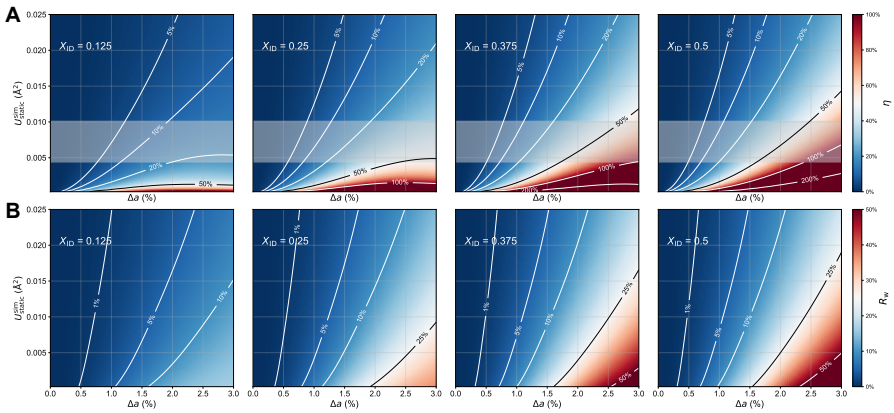

Figure 6.8: (**A**) The distribution of the error (η) of LLDs. Each pixel point corresponds to a value of the difference between LLDs from simulated and fitted PDFs. The colour scale indicates the magnitude of the error, with red indicating large errors while blue indicates small errors. The contour lines represent the same error value. The translucent regions show the typical U_{static} range in RHEAs. (**B**) R_{w} values as an indicator of the fitting quality. The colour scale indicates their magnitude, with red representing poor fits and blue representing good fits, while the white and black lines are iso-R_{w} contours. *This figure is reproduced from Ref. [107], licensed under the Creative Commons CC BY license.*

red and blue curves). Fitting the composite PDFs, particularly those with large lattice parameter differences, to a single-phase model leads to significant deviations from the model, as shown in Figure 6.7B and C.

The error, η, is plotted as a function of Δa and $U^{\text{sim}}_{\text{static}}$ for each molar fraction in Figure 6.8A, where the red regions indicate greater errors, i.e., where fitting results are inaccurate. In general, the error increases with increasing lattice parameter difference and decreasing magnitude of $U^{\text{sim}}_{\text{static}}$, as both of these characteristics will lead to more pronounced "separation" of the individual PDFs. It is noted that the error distribution does not follow a monotonic increasing trend, especially for $X_{\text{ID}} < 0.5$. Instead, an unexpected reduction in the rate of increase occurs at regions with low $U^{\text{sim}}_{\text{static}}$ and large Δa values, likely due to the poor fitting quality, as shown in Figure 6.8B. The reduction does not indicate improved accuracy in the extracted LLDs, rather, it is an artifact in a range where the fitting parameters lose physical meaning. An example is shown in Figure 6.7B, where an exceedingly large R_{w} value of 69.0% suggests that the derived parameters may not hold any physical meaning.

A reasonably accurate estimate for the investigated RHEAs (shown by the translucent band in Figure 6.8A) seems to be around $\Delta a \lesssim 1\%$, where both η and R_{w} present relatively low values. But only a small subset of the examined RHEAs satisfies this condition (see details in Paper II), and for most segregated RHEAs the lattice parameter difference Δa is unknown. To draw further conclusion, high-resolution diffraction experiments are needed to

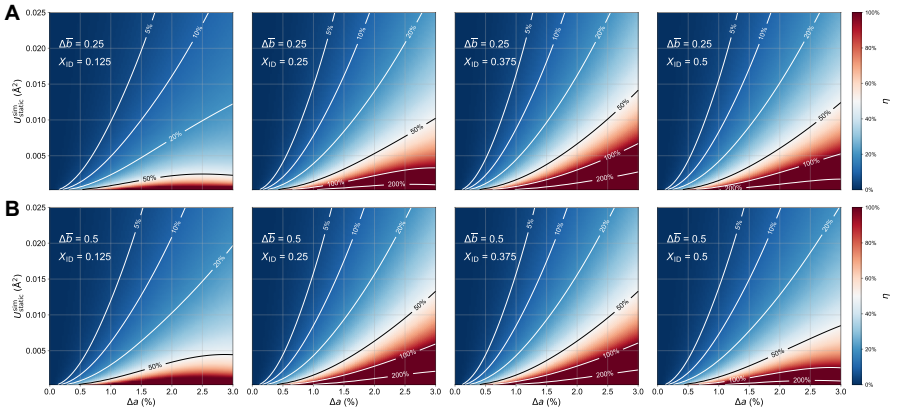

Figure 6.9: Visualisation of the impact of average scattering length differences ($\Delta\bar{b}$) and molar fraction (X_{ID}) on error determination. The scattering length of the interdendritic regions was varied to differ by (**A**) 25% and (**B**) 50% relative to that of the dendrites. *This figure is reproduced from Ref. [107], licensed under the Creative Commons CC BY license.*

determine Δa for a broader range of RHEAs. It should also be noted that this is rather an idealised scenario where all instrumental parameters are assumed to be known, which is not the case in reality.

In previous simulations, the scattering lengths for the two "phases" within the RHEAs were simplified to be identical. However, RHEAs can exhibit relatively large differences in average scattering lengths between dendrites and interdendritic regions (e.g., NbTaTiV and MoNbTaTiV, see details in Paper II). To investigate the effect of average scattering length difference on LLD errors, similar simulations were performed, but specifically with average scattering length differences of 25% ($\Delta\bar{b} = (\bar{b}_2 - \bar{b}_1)/\bar{b}_1 = 0.25$) and 50% ($\Delta\bar{b} = 0.5$). The resulting error is plotted in Figure 6.9. The effect of the scattering length difference is relatively small when compared with the errors in Figure 6.8.

In this section, composite PDFs were simulated for a HfNbTaTiZr RHEA and other segregated RHEAs to explore the validity of using single-phase model for the LLD determination. The results show that the effect of segregation is negligible for HfNbTaTiZr, while in general cases significant inaccuracies could arise under certain conditions, with the errors being dependent on both the extent of segregation and the magnitude of LLDs. Moreover, the simulations suggest that the impact of scattering length differences plays a minor role in the determination of LLDs.

6.4 Temperature dependence of LLDs in RHEAs

As discussed in Section 3.4, current experimental methods for measuring LLDs require the assumption that they are independent of temperature. However, simulation studies have shown that LLDs can exhibit temperature dependence

[55], [56]. More importantly, temperature-induced reductions in LLDs may correlate with increases in elastic moduli with increasing temperatures, which compensates for the modulus reduction caused by thermal expansion and leads to the observation of a temperature-insensitive elastic modulus in a $Co_{25}Ni_{25}(HfTiZr)_{50}$ HEA [57]. Controlling LLDs with temperature appears to be a promising route for tuning certain high-temperature phenomena, for example, the Elinvar effect that is valuable in many industrial applications. Experimental confirmation of the temperature dependence of LLDs could also help eliminate uncertainties on their proposed role in resisting high-temperature softening [54] as well as the role of LLDs in soft-phonon mode suppression and phase stabilisation [13]. In this section, the temperature dependence of LLDs is derived by determining the thermal components from VDOS and specific heat measurements (see Section 6.1.2 and 6.1.3), with the total atomic displacements quantified through neutron total scattering experiments over the cryogenic to room temperature range. A negative temperature dependence of LLDs is observed as a generic feature among the studied bcc-structured RHEAs, suggesting that the widely assumed contribution of LLDs to high-temperature strengthening may need to be reconsidered.

6.4.1 Measurement of total atomic displacements

Three samples were studied to investigate the temperature dependence of LLDs. The first of these is the previously studied HfNbTaTiZr, which exhibits pronounced LLDs. Assuming that LLDs are strongly affected by atomic size mismatch, removing Hf or Zr should lead to a noticeable decrease in the LLDs, therefore NbTaTiZr was included. Finally, MoNbTaW, a prototype RHEA without both Hf and Zr, was studied because Mo and W have relatively high electronegativities compared to the other elements, which could result in strong charge transfer effects thus reducing LLDs.

The total atomic displacements can be determined either by quantifying the intensity decay in diffraction through Rietveld refinement or by quantifying peak broadening in PDF using small-box PDF analysis, both of which yield the atomic displacement parameter U_{iso}, as discussed in Section 4.1.1.5. For a homogeneous HfNbTaTiZr sample, both approaches were applied to variable-temperature neutron total scattering data, and the resulting values differ by less than 5%, as shown in Figure 6.10A.

Figure 6.10B compares the (110) peak of a homogeneous and a heterogeneous HfNbTaTiZr sample where the heterogeneous sample exhibits a broader peak because of the microstructure (as shown in the upper inset) where the segregation of elements to dendritic and interdendritic regions results in slightly different lattice parameters. In contrast, the homogeneous sample in the lower inset shows no such segregation and thus has a narrower peak. Similar microstructure was also observed in MoNbTaW and especially in NbTaTiZr, as shown in Figure 5.1. This affects the real-space analysis more significantly, as the width of the PDF peaks will be broadened [108]. Single-phase small-box fitting will therefore overestimate U_{iso}, and consequently the derived LLDs. The extent of this effect primarily depends on the relative fractions of dendritic

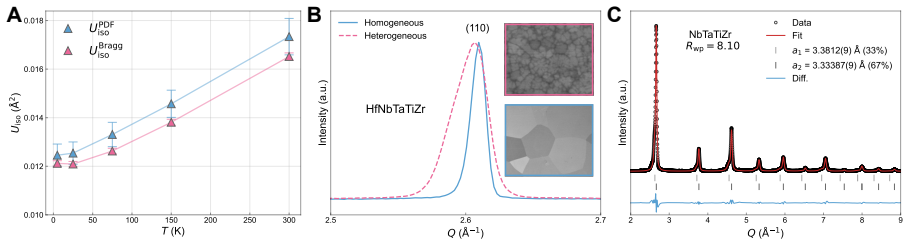

Figure 6.10: (**A**) The atomic displacement parameter U_{iso} as a function of temperature derived from PDF fittings ($U_{\text{iso}}^{\text{PDF}}$) and Rietveld refinements ($U_{\text{iso}}^{\text{Bragg}}$). (**B**) Neutron diffraction pattern of the (110) peak for a homogeneous and a heterogeneous HfNbTaTiZr sample measured on the GEM diffractometer, showing that the heterogeneous sample has a broadened peak. The insets show the microstructure of the two samples. (**C**) Two-phase Rietveld refinement of a high-resolution X-ray diffraction pattern of NbTaTiZr.

and interdendritic regions and the difference in lattice parameter between the two, as discussed in the previous section. A two-phase Rietveld refinement was performed on the high-resolution X-ray diffraction pattern of NbTaTiZr, as shown in Figure 6.10C. The refinement gives a lattice parameter difference of 1.4% between the two phases, with the volume fraction of one phase being 33% and $U_{\text{static}} = 0.0018\text{Å}^2$ (details in Paper IV). After checking against these values to the error map in Figure 6.8A, the error falls in the range of 50–100%, indicating that a single-phase PDF analysis would give highly inaccurate results for this sample. In contrast, the reciprocal-space analysis is less sensitive to segregation, as the effect of the LLDs are seen in the rate of peak intensity decay with Q, which is less affected by the broadened/asymmetric peaks, as their integrated intensity is still relatively well captured in the refinements. Therefore, although the HfNbTaTiZr sample is homogeneous, the total atomic displacements in this study are determined using reciprocal-space Rietveld refinement to ensure consistency across all samples.

Figure 6.11A, B and C show the room-temperature Rietveld refinements of HfNbTaTiZr, NbTaTiZr, and MoNbTaW, respectively. The different magnitude of atomic displacements can be qualitatively seen from the decay of peak intensity with increasing Q in the diffractograms. For HfNbTaTiZr and NbTaTiZr, peaks beyond $Q = 14$ Å^{-1} are nearly absent despite different instrumental resolution, whereas in MoNbTaW the decay is less pronounced, indicating comparatively smaller atomic displacements. Figure 6.11D shows the U_{iso} values across the measured temperatures obtained from Rietveld refinements for the three RHEAs, with the instrumental component $U_{\text{i/p}}$ subtracted (see details in Papers III and IV). The U_{iso} values for MoNbTaW are the lowest of the three as expected, but the reduction in U_{iso} from the removal of Hf is unexpectedly large; this will be discussed in Section 6.4.2.

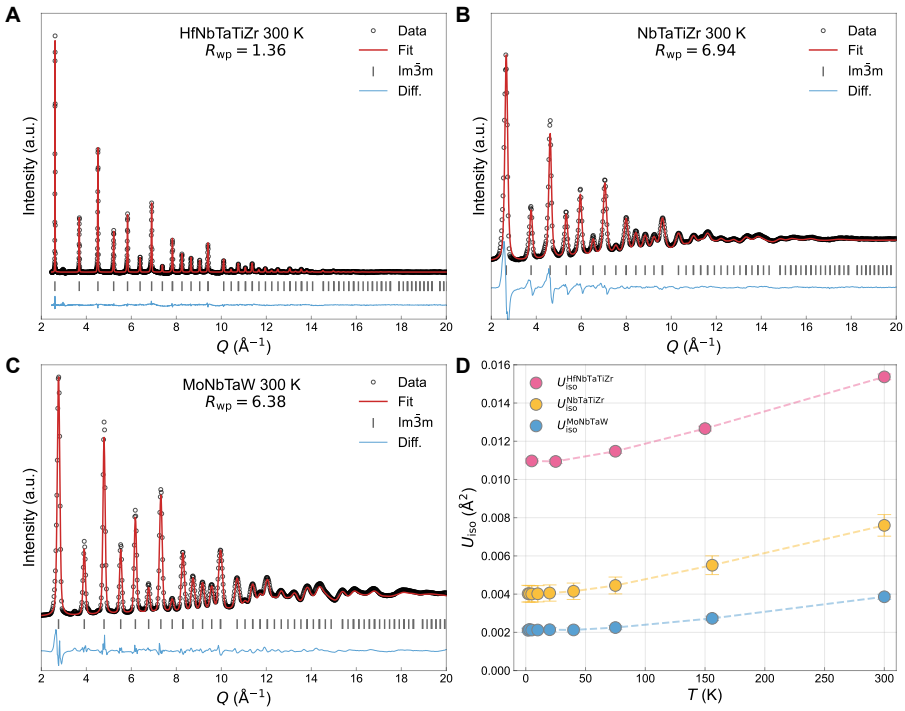

Figure 6.11: Rietveld refinements of (**A**) HfNbTaTiZr, (**B**) NbTaTiZr and (**C**) MoNbTaW at room temperature. Results for the remaining temperatures can be found in Paper III and IV. (**D**) The total atomic displacement parameter U_{iso} extracted from Rietveld refinements across measured temperatures.

6.4.2 Isolation of LLDs

The thermal components were determined in Section 6.1, with the thermal displacements of HfNbTaTiZr obtained from the VDOS and those of NbTaTiZr and MoNbTaW derived from specific heat data using Debye approximation. The corresponding thermal displacement parameters U_{thermal} are compared in Figure 6.12A. The rate of increase in U_{thermal} reflects the differences in their Debye temperatures (233 K for HfNbTaTiZr, 253K for NbTaTiZr and 330 K for MoNbTaW, respectively). Figure 6.12B shows the decomposition of the total displacements into thermal and static components. As expected, HfNbTaTiZr shows the highest σ_{static}, followed by NbTaTiZr and then MoNbTaW. The same trend is observed in the LLDs, as shown in Figure 6.12C. To identify the origins of the variations in the static displacements and LLDs, the atomic size mismatch (δ) and charge transfer effects are quantified. δ is already defined in Equation 3.5; similarly, the difference in electronegativity can be expressed as a relative change:

$$\Delta\chi = \sqrt{\sum_i c_i \left(1 - \frac{\chi_i}{\bar{\chi}}\right)^2}, \tag{6.6}$$

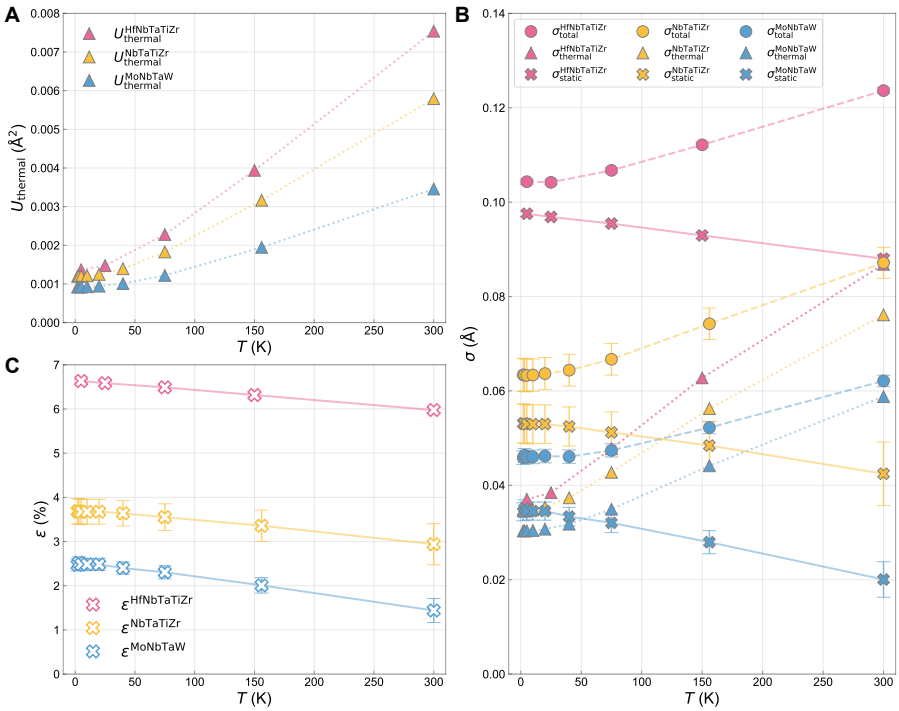

Figure 6.12: Comparison among the three RHEAs of (**A**) the thermal displacement parameters U_{thermal}, (**B**) the different components of the displacements, and (**C**) the LLDs as a function of temperature.

where χ_i is the Pauling-scale electronegativity of element i, and $\bar{\chi} = \sum_i c_i \chi_i$ is the average electronegativity. The calculated values of δ and $\Delta\chi$, together with the low-T ε, are summarised in Table 6.4. The removal of Hf reduces the LLDs in HfNbTaTiZr from 6.6% to 3.7% in NbTaTiZr, despite almost the same δ (4.0% and 3.9%, respectively) and even a decrease in $\Delta\chi$ (8.2% to 7.0%). The exceptionally large LLDs in the Hf-containing alloy may be related to the soft bonding associated with Hf due to its low elastic modulus, the

Table 6.4: Comparison of atomic size mismatch (δ, using atomic radii from [109]), electronegativity difference parameter ($\Delta\chi$, using Pauling scale) and LLD (ε, at low-T) among the studied alloys.

Alloys	δ (%)	$\Delta\chi$ (%)	ε (%)
HfNbTaTiZr	4.0	8.2	6.6
NbTaTiZr	3.9	7.0	3.7
MoNbTaW	2.3	19.2	2.5

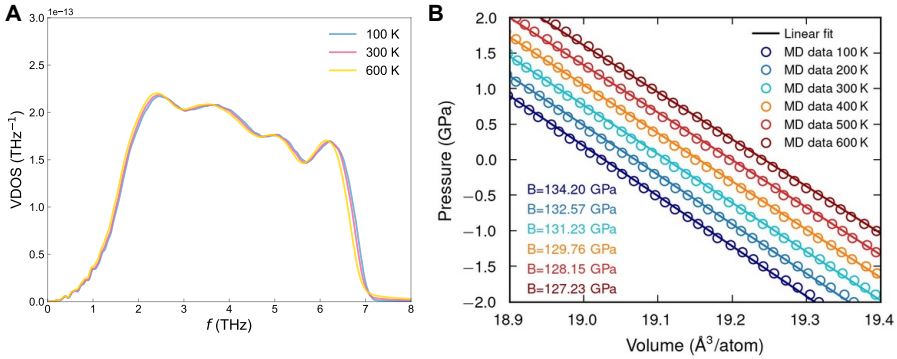

Figure 6.13: (**A**) VDOS of HfNbTaTiZr at 100, 300 and 600 K show negligible difference, indicating a weak temperature dependence. (**B**) The bulk modulus of HfNbTaTiZr as a function of temperature also show a weak temperature dependence.

evidence of which is currently lacking in the metastable bcc structure of these hcp-derived elements. On the other hand, replacing Ti and Zr with Mo and W not only lowers the atomic size mismatch (to a small value of 2.3%), but also significantly increases $\Delta\chi$ to 19.2%. The enhanced electronegativity difference likely promotes stronger charge transfer effects, which help mitigate LLDs and lead to the lowest ε value of 2.5% in MoNbTaW. In addition, a general negative temperature dependence of LLDs is observed in all investigated RHEAs, and the rate of decrease with temperature is roughly independent of composition. The origin of the temperature dependence of LLDs remains unclear at this stage. Because charge transfer is only weakly dependent on temperature, and thermal expansion in metals is small, neither effect can explain the observed 10–40% relative reduction in LLDs from cryogenic to room temperature (see Paper IV). The nearly temperature-independent VDOS curves of HfNbTaTiZr (Figure 6.13A), and the weak temperature dependence of its bulk modulus (Figure 6.13B), suggest a minimal thermal softening of the lattice. Although Ti and Zr exhibit pronounced modulus decreases with temperature in their stable phases [110], their behaviour within the bcc structure is still unknown and requires further study.

6.5 Conclusions and Outlook

In this thesis, LLDs in RHEAs were quantified with scattering-based techniques. Based on the results, the following conclusions can be drawn:

- Rietveld refinement results are consistent with small-box PDF analysis for quantifying LLDs, and LLDs are measured to be severe in bcc-structured RHEAs compared to their fcc counterparts.
- Segregation can significantly affect the accuracy of LLD determinations in certain scenarios. Specifically, care must be taken when the difference in lattice parameters between the segregated regions is large and the level of static displacement is low, which is where the errors in LLD measurements become pronounced. Determining U_{iso} from reciprocal-space refinements is a more suitable approach in this case.
- Separation of thermal displacements is necessary for extracting the temperature dependence information of LLDs. For the RHEAs studied here, thermal displacements from VDOS and specific heat measurements are in good agreement.
- A negative temperature dependence of LLDs is observed in all investigated RHEAs and is independent of compositio, perhaps because of the temperature dependence of the elastic modulus of certain elements.

Building on the findings and discussions presented, several promising directions for future work can be identified:

- For heterogeneous alloys, determining U_{iso} from reciprocal-space refinements appears to be more suitable than determining from real-space analysis. A similar simulation study on reciprocal-space-based LLD characterisation in segregated structure would be useful for quantifying the errors.
- Although LLDs are often attributed to a strengthening mechanism in RHEAs, their magnitude has been shown to decrease with temperature. Since RHEAs are intended for high-temperature applications (where LLDs may be substantially reduced) their actual relevance to high-temperature mechanical property remains uncertain. To clarify this, measuring LLDs at elevated temperatures are needed.
- Direct measurement of the generalised phonon density of states (GDOS) using inelastic neutron scattering would provide a validation of the actual vibrational behaviour in the RHEAs.

Bibliography

[1] J. W. Yeh, S. K. Chen, S. J. Lin, J. Y. Gan, T. S. Chin, T. T. Shun, C. H. Tsau and S. Y. Chang, Nanostructured high-entropy alloys with multiple principal elements: Novel alloy design concepts and outcomes, *Adv. Eng. Mater.*, **6**, 299–303 (2004).

[2] B. Cantor, I. T. Chang, P. Knight and A. J. Vincent, Microstructural development in equiatomic multicomponent alloys, *Mater. Sci. Eng. A*, **375-377**, 213–218 (2004).

[3] E. P. George, D. Raabe and R. O. Ritchie, High-entropy alloys, *Nat. Rev. Mater.*, **4**, 515–534 (2019).

[4] D. B. Miracle and O. N. Senkov, A critical review of high entropy alloys and related concepts, *Acta Mater.*, **122**, 448–511 (2017).

[5] O. N. Senkov, G. B. Wilks, J. M. Scott and D. B. Miracle, Mechanical properties of Nb25Mo25Ta 25W25 and V20Nb20Mo 20Ta20W20 refractory high entropy alloys, *Intermetallics*, **19**, 698–706 (2011).

[6] S. S. Sohn, A. Kwiatkowski da Silva, Y. Ikeda, F. Körmann, W. Lu, W. S. Choi, B. Gault, D. Ponge, J. Neugebauer and D. Raabe, Ultrastrong Medium-Entropy Single-Phase Alloys Designed via Severe Lattice Distortion, *Adv. Mater.*, **31**, 1–8 (2019).

[7] Z. Wang, Q. Fang, J. Li, B. Liu and Y. Liu, Effect of lattice distortion on solid solution strengthening of BCC high-entropy alloys, *J. Mater. Sci. Technol.*, **34**, 349–354 (2018).

[8] B. Chen, S. Li, J. Ding, X. Ding, J. Sun and E. Ma, Correlating dislocation mobility with local lattice distortion in refractory multi-principal element alloys, *Scr. Mater.*, **222**, 115048 (2023).

[9] F. Wang, G. H. Balbus, S. Xu, Y. Su, J. Shin, P. F. Rottmann, K. E. Knipling, J.-C. Stinville, L. H. Mills, O. N. Senkov, I. J. Beyerlein, T. M. Pollock and D. S. Gianola, Multiplicity of dislocation pathways in a refractory multiprincipal element alloy, *Science*, **370**, 95–101 (2020).

[10] D. B. Miracle, J. D. Miller, O. N. Senkov, C. Woodward, M. D. Uchic and J. Tiley, Exploration and development of high entropy alloys for structural applications, *Entropy*, **16**, 494–525 (2014).

[11] Q. J. Li, H. Sheng and E. Ma, Strengthening in multi-principal element alloys with local-chemical-order roughened dislocation pathways, *Nat. Commun.*, **10**, 1–11 (2019).

[12] J. W. Yeh, Recent progress in high-entropy alloys, *Ann. Chim. Sci. des Mater.*, **31**, 633–648 (2006).

[13] G. D. Samolyuk, Y. N. Osetsky, G. M. Stocks and J. R. Morris, Role of Static Displacements in Stabilizing Body Centered Cubic High Entropy Alloys, *Phys. Rev. Lett.*, **126**, 025501 (2021).

[14] H. Wang, Q. He, X. Gao, Y. Shang, W. Zhu, W. Zhao, Z. Chen, H. Gong and Y. Yang, Multifunctional High Entropy Alloys Enabled by Severe Lattice Distortion, *Adv. Mater.*, **36**, 1–20 (2024).

[15] O. N. Senkov, J. M. Scott, S. V. Senkova, F. Meisenkothen, D. B. Miracle and C. F. Woodward, Microstructure and elevated temperature properties of a refractory TaNbHfZrTi alloy, *J. Mater. Sci.*, **47**, 4062–4074 (2012).

[16] O. N. Senkov, J. M. Scott, S. V. Senkova, D. B. Miracle and C. F. Woodward, Microstructure and room temperature properties of a high-entropy TaNbHfZrTi alloy, *J. Alloys Compd.*, **509**, 6043–6048 (2011).

[17] O. N. Senkov, G. B. Wilks, D. B. Miracle, C. P. Chuang and P. K. Liaw, Refractory high-entropy alloys, *Intermetallics*, **18**, 1758–1765 (2010).

[18] D. B. Miracle, M. H. Tsai, O. N. Senkov, V. Soni and R. Banerjee, Refractory high entropy superalloys (RSAs), *Scr. Mater.*, **187**, 445–452 (2020).

[19] Z. D. Han, H. W. Luan, X. Liu, N. Chen, X. Y. Li, Y. Shao and K. F. Yao, Microstructures and mechanical properties of TixNbMoTaW refractory high-entropy alloys, *Mater. Sci. Eng. A*, **712**, 380–385 (2018).

[20] L. Qi and D. C. Chrzan, Tuning ideal tensile strengths and intrinsic ductility of bcc refractory alloys, *Phys. Rev. Lett.*, **112**, 1–5 (2014).

[21] G. Dirras, L. Lilensten, P. Djemia, M. Laurent-Brocq, D. Tingaud, J. P. Couzinié, L. Perrière, T. Chauveau and I. Guillot, Elastic and plastic properties of as-cast equimolar TiHfZrTaNb high-entropy alloy, *Mater. Sci. Eng. A*, **654**, 30–38 (2016).

[22] S. Sheikh, S. Shafeie, Q. Hu, J. Ahlström, C. Persson, J. Veselý, J. Zýka, U. Klement and S. Guo, Alloy design for intrinsically ductile refractory high-entropy alloys, *J. Appl. Phys.*, **120**, 164902 (2016).

[23] Y. D. Wu, Y. H. Cai, T. Wang, J. J. Si, J. Zhu, Y. D. Wang and X. D. Hui, A refractory Hf25Nb25Ti25Zr25 high-entropy alloy with excellent structural stability and tensile properties, *Mater. Lett.*, **130**, 277–280 (2014).

[24] H. Huang, Y. Wu, J. He, H. Wang, X. Liu, K. An, W. Wu and Z. Lu, Phase-Transformation Ductilization of Brittle High-Entropy Alloys via Metastability Engineering, *Adv. Mater.*, **29**, 1–7 (2017).

[25] W. Benenson, J. W. Harris, H. Stocker and H. Lutz, *Handbook of Physics*. Springer New York, 2002, pp. 1–1185, ISBN: 978-0-387-95269-7.

[26] Y. Tong, S. Zhao, H. Bei, T. Egami, Y. Zhang and F. Zhang, Severe local lattice distortion in Zr- and/or Hf-containing refractory multi-principal element alloys, *Acta Mater.*, **183**, 172–181 (2020).

[27] F. Lukac, M. Dudr, R. Musalek, J. Klecka, J. Cinert, J. Cizek, T. Chraska, J. Cizek, O. Melikhova, J. Kuriplach, J. Zyka and J. Malek, Spark plasma sintering of gas atomized high-entropy alloy HfNbTaTiZr, *J. Mater. Res.*, **33**, 3247–3257 (2018).

[28] M. Wang, Z. L. Ma, Z. Q. Xu and X. W. Cheng, Designing VxNbMoTa refractory high-entropy alloys with improved properties for high-temperature applications, *Scr. Mater.*, **191**, 131–136 (2021).

[29] L. R. Owen and N. G. Jones, Lattice distortions in high-entropy alloys, *J. Mater. Res.*, **33**, 2954–2969 (2018).

[30] H. Song, F. Tian, Q. M. Hu, L. Vitos, Y. Wang, J. Shen and N. Chen, Local lattice distortion in high-entropy alloys, *Phys. Rev. Mater.*, **1**, 23404 (2017).

[31] L. Y. Tian, G. Wang, J. S. Harris, D. L. Irving, J. Zhao and L. Vitos, Alloying effect on the elastic properties of refractory high-entropy alloys, *Mater. Des.*, **114**, 243–252 (2017).

[32] H. Ge and F. Tian, A Review of Ab Initio Calculation on Lattice Distortion in High-Entropy Alloys, *Jom*, **71**, 4225–4237 (2019).

[33] L. R. Owen and N. G. Jones, Quantifying local lattice distortions in alloys, *Scr. Mater.*, **187**, 428–433 (2020).

[34] L. Owen, N. Jones, H. Stone and H. Playford, Separation of static and dynamic displacements in the CrMnFeCoNi high entropy alloy, *Acta Mater.*, **262**, 119164 (2024).

[35] L. Casillas-Trujillo, B. Osinger, R. Lindblad, D. Karlsson, A. I. Abrikosov, S. Fritze, K. Von Fieandt, B. Alling, I. Hotz, U. Jansson, I. A. Abrikosov and E. Lewin, Experimental and theoretical evidence of charge transfer in multi-component alloys-how chemical interactions reduce atomic size mismatch, *Mater. Chem. Front.*, **5**, 5746–5759 (2021).

[36] F. Meng, W. Zhang, Z. Zhou, R. Sheng, A. C. Chuang, C. Wu, H. Huang, S. Zhang, H. Zhang, L. Zhu, L. Jiang, P. K. Liaw, S. Chen and Y. Tong, Charge transfer effect on local lattice distortion in a HfNbTiZr high entropy alloy, *Scr. Mater.*, **203**, 114104 (2021).

[37] Y. Tong and F. Zhang, Critical Review of Chemical Complexity Effect on Local Structure of Multi-principal-Element Alloys, *JOM*, **71**, 3419–3423 (2019).

[38] S. Mu, R. J. Olsen, B. Dutta, L. Lindsay, G. D. Samolyuk, T. Berlijn, E. D. Specht, K. Jin, H. Bei, T. Hickel, B. C. Larson and G. M. Stocks, Unfolding the complexity of phonon quasi-particle physics in disordered materials, *npj Comput. Mater.*, 1–8 (2020).

[39] S. R. Turner, S. Pailhès, F. Bourdarot, J. Ollivier, Y. Sidis, J.-P. Castellan, J.-M. Zanotti, Q. Berrod, F. Porcher, A. Bosak, M. Feuerbacher, H. Schober, M. de Boissieu and V. M. Giordano, Phonon behavior in a random solid solution: a lattice dynamics study on the high-entropy alloy FeCoCrMnNi, *Nat. Commun.*, **13**, 7509 (2022).

[40] F. Körmann, Y. Ikeda, B. Grabowski and M. H. Sluiter, Phonon broadening in high entropy alloys, *npj Comput. Mater.*, **3**, 1–8 (2017).

[41] C. Lee, Y. Chou, G. Kim, M. C. Gao, K. An, J. Brechtl, C. Zhang, W. Chen, J. D. Poplawsky, G. Song, Y. Ren, Y. C. Chou and P. K. Liaw, Lattice-Distortion-Enhanced Yield Strength in a Refractory High-Entropy Alloy, *Adv. Mater.*, **32**, 2004029 (2020).

[42] P. Thirathipviwat, S. Sato, G. Song, J. Bednarcik, K. Nielsch, J. Jung and J. Han, A role of atomic size misfit in lattice distortion and solid solution strengthening of TiNbHfTaZr high entropy alloy system, *Scr. Mater.*, **210**, 114470 (2022).

[43] B. Chen, S. Li, H. Zong, X. Ding, J. Sun and E. Ma, Unusual activated processes controlling dislocation motion in body-centered-cubic high-entropy alloys, *PNAS*, **117**, 16199–161206 (2020).

[44] C. Lee, F. Maresca, R. Feng, Y. C. Chou, T. Ungar, M. Widom, K. An, J. D. Poplawsky, Y. C. Chou, P. K. Liaw and W. A. Curtin, Strength can be controlled by edge dislocations in refractory high-entropy alloys, *Nat. Commun.*, **12**, 5474 (2021).

[45] P. P. Borges, R. O. Ritchie and M. Asta, Local lattice distortions and the structural instabilities in bcc Nb–Ta–Ti–Hf high-entropy alloys: An ab initio computational study, *Acta Mater.*, **262**, 119415 (2024).

[46] S. Mu, S. Wimmer, S. Mankovsky, H. Ebert and G. M. Stocks, Influence of local lattice distortions on electrical transport of refractory high entropy alloys, *Scr. Mater.*, **170**, 189–194 (2019).

[47] K. Jasiewicz, J. Tobola and B. Wiendlocha, Local distortions of the crystal structure and their influence on the electronic structure and superconductivity of the high-entropy alloy (TaNb)0.67(HfZrTi)0.33, *Phys. Rev. B*, **108**, 224505 (2023).

[48] P. Koželj, S. Vrtnik, A. Jelen, S. Jazbec, Z. Jagličić, S. Maiti, M. Feuerbacher, W. Steurer and J. Dolinšek, Discovery of a Superconducting High-Entropy Alloy, *Phys. Rev. Lett.*, **113**, 107001 (2014).

[49] S. Vrtnik, P. Koželj, A. Meden, S. Maiti, W. Steurer, M. Feuerbacher and J. Dolinšek, Superconductivity in thermally annealed Ta-Nb-Hf-Zr-Ti high-entropy alloys, *J. Alloys Compd.*, **695**, 3530–3540 (2017).

[50] Z. Fan, H. Wang, Y. Wu, X. J. Liu and Z. P. Lu, Thermoelectric high-entropy alloys with low lattice thermal conductivity, *RSC Adv.*, **6**, 52164–52170 (2016).

[51] B. Jiang, Y. Yu, J. Cui, X. Liu, L. Xie, J. Liao, Q. Zhang, Y. Huang, S. Ning, B. Jia, B. Zhu, S. Bai, L. Chen, S. J. Pennycook and J. He, High-entropy-stabilized chalcogenides with high thermoelectric performance, *Science*, **371**, 830–834 (2021).

[52] F. Zhang, Y. Tong, K. Jin, H. Bei, W. J. Weber, A. Huq, A. Lanzirotti, M. Newville, D. C. Pagan, J. Y. P. Ko and Y. Zhang, Chemical complexity induced local structural distortion in NiCoFeMnCr high-entropy alloy, *Mater. Res. Lett.*, **6**, 450–455 (2018).

[53] Z. Tian, J. Y. Law, L. M. Moreno-Ramírez, Y. Liu, F. Hu, A. G. Gamzatov, A. Aliev, A. Kadirbardeev, J. Wang, W. Zhai, B. Wei, V. Franco and B. Shen, Compositionally complex alloying in multiple-R-Co2 laves phase system: Lattice distortion and static and dynamic magnetocaloric properties, *Acta Mater.*, **299**, 121472 (2025).

[54] C. Lee, G. Song, M. C. Gao, R. Feng, P. Chen, J. Brechtl, Y. Chen, K. An, W. Guo, J. D. Poplawsky, S. Li, A. T. Samaei, W. Chen, A. Hu, H. Choo and P. K. Liaw, Lattice distortion in a strong and ductile refractory high-entropy alloy, *Acta Mater.*, **160**, 158–172 (2018).

[55] D. Utt, A. Stukowski and K. Albe, Grain boundary structure and mobility in high-entropy alloys: A comparative molecular dynamics study on a Σ11 symmetrical tilt grain boundary in face-centered cubic CuNiCoFe, *Acta Mater.*, **186**, 11–19 (2020).

[56] H. Chen, Y. Xu, L. Liu, Y. Chen, J. Wróbel, D. Cong, F. Tian and Y. Wang, Lattice distortion tuning resistivity Invar effect in high-entropy alloys, *Phys. Rev. B*, **111**, 094209 (2025).

[57] Q. F. He, J. G. Wang, H. A. Chen, Z. Y. Ding, Z. Q. Zhou, L. H. Xiong, J. H. Luan, J. M. Pelletier, J. C. Qiao, Q. Wang, L. L. Fan, Y. Ren, Q. S. Zeng, C. T. Liu, C. W. Pao, D. J. Srolovitz and Y. Yang, A highly distorted ultraelastic chemically complex Elinvar alloy, *Nature*, **602**, 251–257 (2022).

[58] H. Wang, Q. F. He, A. D. Wang and Y. Yang, Tuning Elinvar effect in severely distorted single-phase high entropy alloys, *J. Appl. Phys.*, **133** (2023).

[59] T. Egami and S. J. Billinge, *Underneath the Bragg Peaks: Structural Analysis of Complex Materials*. Elsevier Ltd., 2012, vol. 16, pp. 2–481, ISBN: 978-0-08-097133-9.

[60] D. A. Keen, A comparison of various commonly used correlation functions for describing total scattering, *J. Appl. Crystallogr.*, **34**, 172–177 (2001).

[61] C. L. Farrow, P. Juhas, J. W. Liu, D. Bryndin, E. S. Boin, J. Bloch, T. Proffen and S. J. Billinge, PDFfit2 and PDFgui: Computer programs for studying nanostructure in crystals, *J. Phys. Condens. Matter*, **19**, 335219 (2007).

[62] P. Juhás, C. L. Farrow, X. Yang, K. R. Knox and S. J. Billinge, Complex modeling: A strategy and software program for combining multiple information sources to solve ill posed structure and nanostructure inverse problems, *Acta Crystallogr. Sect. A Found. Adv.*, **71**, 562–568 (2015).

[63] A. Béché, J. L. Rouvière, J. P. Barnes and D. Cooper, Dark field electron holography for strain measurement, *Ultramicroscopy*, **111**, 227–238 (2011).

[64] J. Li, Y. Chen, Q. He, X. Xu, H. Wang, C. Jiang, B. Liu, Q. Fang, Y. Liu, Y. Yang, P. K. Liaw and C. T. Liu, Heterogeneous lattice strain strengthening in severely distorted crystalline solids, *PNAS*, **119**, 1–7 (2022).

[65] Y. Zou, S. Maiti, W. Steurer and R. Spolenak, Size-dependent plasticity in an Nb25Mo25Ta 25W25 refractory high-entropy alloy, *Acta Mater.*, **65**, 85–97 (2014).

[66] V. B. Ozdol, C. Gammer, X. G. Jin, P. Ercius, C. Ophus, J. Ciston and A. M. Minor, Strain mapping at nanometer resolution using advanced nano-beam electron diffraction, *Appl. Phys. Lett.*, **106** (2015).

[67] Y.-T. Shao, R. Yuan, H.-W. Hsiao, Q. Yang, Y. Hu and J.-M. Zuo, Cepstral scanning transmission electron microscopy imaging of severe lattice distortions, *Ultramicroscopy*, **231**, 113252 (2021).

[68] M. Hÿtch, C. Gatel, F. Houdellier, E. Snoeck and K. Ishizuka, Darkfield electron holography for strain mapping at the nanoscale, *Microsc. Anal.*, **26**, 6–10 (2012).

[69] H. S. Oh, D. Ma, G. P. Leyson, B. Grabowski, E. S. Park, F. Kormann and D. Raabe, Lattice distortions in the FeCoNiCrMn high entropy alloy studied by theory and experiment, *Entropy*, **18**, 321 (2016).

[70] Y.-Y. Tan, M.-Y. Su, Z.-C. Xie, Z.-J. Chen, Y. Gong, L.-R. Zheng, Z. Shi, G. Mo, Y. Li, L.-W. Li, H.-Y. Wang and L.-H. Dai, Chemical composition dependent local lattice distortions and magnetism in high entropy alloys, *Intermetallics*, **129**, 107050 (2021).

[71] Y. Y. Tan, T. Li, Y. Chen, Z. J. Chen, M. Y. Su, J. Zhang, Y. Gong, T. Wu, H. Y. Wang and L. H. Dai, Uncovering heterogeneity of local lattice distortion in TiZrHfNbTa refractory high entropy alloy by SR-XRD and EXAFS, *Scr. Mater.*, **223**, 115079 (2023).

[72] A. Fantin, G. O. Lepore, A. M. Manzoni, S. Kasatikov, T. Scherb, T. Huthwelker, F. D'Acapito and G. Schumacher, Short-range chemical order and local lattice distortion in a compositionally complex alloy, *Acta Mater.*, **193**, 329–337 (2020).

[73] A. Fantin, A. M. Manzoni, H. Springer, R. D. Kamachali and R. Maaß, Local lattice distortions and chemical short-range order in MoNbTaW, *Mater. Res. Lett.*, **12**, 346–354 (2024).

[74] P. Debye, Zur Theorie der spezifischen Wärmen, *Ann. Phys.*, **344**, 789–839 (1912).

[75] B. T. M. Wills and A. W. Pryor, *Thermal vibrations in crystallography.* Cambridge University Press, 1975, ISBN: 052120447X.

[76] S. Y. Chen, Y. Tong, K. K. Tseng, J. W. Yeh, J. D. Poplawsky, J. G. Wen, M. C. Gao, G. Kim, W. Chen, Y. Ren, R. Feng, W. D. Li and P. K. Liaw, Phase transformations of HfNbTaTiZr high-entropy alloy at intermediate temperatures, *Scr. Mater.*, **158**, 50–56 (2019).

[77] R. Langford and M. Rogers, In situ lift-out: Steps to improve yield and a comparison with other FIB TEM sample preparation techniques, *Micron*, **39**, 1325–1330 (2008).

[78] K. Thompson, D. Lawrence, D. Larson, J. Olson, T. Kelly and B. Gorman, In situ site-specific specimen preparation for atom probe tomography, *Ultramicroscopy*, **107**, 131–139 (2007).

[79] A. C. Dippel, H. P. Liermann, J. T. Delitz, P. Walter, H. Schulte-Schrepping, O. H. Seeck and H. Franz, Beamline P02.1 at PETRA III for high-resolution and high-energy powder diffraction, *J. Synchrotron Radiat.*, **22**, 675–687 (2015).

[80] M. V Zimmermann, O. Ivashko, F. Igoa Saldaña, J. Liu, P. Glaevecke, O. Gutowski, R. Nowak, K. Köhler, B. Winkler, A. Schöps, H. Schulte-Schrepping and A. C. Dippel, P21.1 at PETRA III - a high-energy X-ray diffraction beamline for physics and chemistry, *J. Synchrotron Radiat.*, **32**, 802–814 (2025).

[81] Z. Hegedüs, T. Müller, J. Hektor, E. Larsson, T. Bäcker, S. Haas, A. L. Conceiçao, S. Gutschmidt and U. Lienert, Imaging modalities at the Swedish Materials Science beamline at PETRA III, *IOP Conf. Ser. Mater. Sci. Eng.*, **580** (2019).

[82] A. C. Hannon, Results on disordered materials from the GEneral Materials diffractometer, GEM, at ISIS, *Nucl. Instruments Methods Phys. Res. Sect. A Accel. Spectrometers, Detect. Assoc. Equip.*, **551**, 88–107 (2005).

[83] W. Williams, R. Ibberson, P. Day and J. Enderby, GEM — General materials diffractometer at ISIS, *Phys. B Condens. Matter*, **241-243**, 234–236 (1997).

[84] H. E. Fischer, G. J. Cuello, P. Palleau, D. Feltin, A. C. Barnes, Y. S. Badyal and J. M. Simonson, D4c: A very high precision diffractometer for disordered materials, *Appl. Phys. A Mater. Sci. Process.*, **74**, 160–162 (2002).

[85] J. Kieffer, J. Orlans, N. Coquelle, S. Debionne, S. Basu, A. Homs, G. Santoni and D. De Sanctis, Application of signal separation to diffraction image compression and serial crystallography, *J. Appl. Crystallogr.*, **58**, 138–153 (2025).

[86] P. Juhás, T. Davis, C. L. Farrow and S. J. L. Billinge, PDFgetX3 : a rapid and highly automatable program for processing powder diffraction data into total scattering pair distribution functions, *J. Appl. Crystallogr.*, **46**, 560–566 (2013).

[87] V. F. Sears, Neutron scattering lengths and cross sections, *Neutron News*, **3**, 26–37 (1992).

[88] A. Soper, GudrunN and GudrunX: Programs for Correcting Raw Neutron and X-ray Diffraction Data to Differential Scattering Cross Section, *RAL Rep. RAL-TR-2011-013*, 1–151 (2011).

[89] F. Akeroyd, S. Ansell, S. Antony, O. Arnold, A. Bekasovs, J. Bilheux, J. Borreguero, K. Brown, A. Buts, S. Campbell, D. Champion, L. Chapon, M. Clarke, S. Cottrell, R. Dalgliesh, D. Dillow, M. Dou, W. Zhou and J. Zikovsky, Mantid: Manipulation and Analysis Toolkit for Instrument Data, *Mantid Proj.* (2013).

[90] O. Arnold, J. C. Bilheux, J. M. Borreguero, A. Buts, S. I. Campbell, L. Chapon, M. Doucet, N. Draper, R. Ferraz Leal, M. A. Gigg, V. E. Lynch, A. Markvardsen, D. J. Mikkelson, R. L. Mikkelson, R. Miller, K. Palmen, P. Parker, G. Passos, T. G. Perring, P. F. Peterson, S. Ren, M. A. Reuter, A. T. Savici, J. W. Taylor, R. J. Taylor, R. Tolchenov, W. Zhou and J. Zikovsky, Mantid - Data analysis and visualization package for neutron scattering and μ SR experiments, *Nucl. Instruments Methods Phys. Res. Sect. A Accel. Spectrometers, Detect. Assoc. Equip.*, **764**, 156–166 (2014).

[91] P. Juhás, J. N. Louwen, L. van Eijck, E. T. C. Vogt and S. J. L. Billinge, PDFgetN3: atomic pair distribution functions from neutron powder diffraction data using ad hoc corrections, *J. Appl. Crystallogr.*, **51**, 1492–1497 (2018).

[92] A. A. Coelho, TOPAS and TOPAS-Academic: An optimization program integrating computer algebra and crystallographic objects written in C++: An, *J. Appl. Crystallogr.*, **51**, 210–218 (2018).

[93] B. H. Toby and R. B. Von Dreele, GSAS-II: The genesis of a modern open-source all purpose crystallography software package, *J. Appl. Crystallogr.*, **46**, 544–549 (2013).

[94] H. M. Rietveld, A profile refinement method for nuclear and magnetic structures, *J. Appl. Crystallogr.*, **2**, 65–71 (1969).

[95] M. G. Tucker, D. A. Keen, M. T. Dove, A. L. Goodwin and Q. Hui, RMCProfile: Reverse Monte Carlo for polycrystalline materials, *J. Phys. Condens. Matter*, **19**, 335218 (2007).

[96] Y. Zhang, M. Eremenko, V. Krayzman, M. G. Tucker and I. Levin, New capabilities for enhancement of RMCProfile: Instrumental profiles with arbitrary peak shapes for structural refinements using the reverse Monte Carlo method, *J. Appl. Crystallogr.*, **53**, 1509–1518 (2020).

[97] L. R. Owen, 'The analysis of local structural effects in alloys using total scattering and reverse Monte Carlo techniques,' Ph.D. dissertation, University of Cambridge, 2017, p. 238.

[98] O. N. Senkov, S. Gorsse and D. B. Miracle, High temperature strength of refractory complex concentrated alloys, *Acta Mater.*, **175**, 394–405 (2019).

[99] L. M. Peng, G. Ren, S. L. Dudarev and M. J. Whelan, Debye-Waller factors and absorptive scattering factors of elemental crystals, *Acta Crystallogr. Sect. A Found. Crystallogr.*, **52**, 456–470 (1996).

[100] M. Shankar Narayana, N. Gopi Krishna and D. B. Sirdeshmukh, X-ray determination of Debye–Waller factors and Debye temperatures of h.c.p. elements Ti, Zr, Ru, Tm, Hf, *Acta Crystallogr. Sect. A Found. Crystallogr.*, **57**, 217–218 (2001).

[101] E. Purushotham and N. Gopi Krishna, Mean square amplitudes of vibration and associated Debye temperatures of rhenium, osmium and thallium, *Phys. B Condens. Matter*, **405**, 3308–3311 (2010).

[102] Y. Hu, L. R. Owen, H. Y. Playford, A. Edgren, S. Guo and M. H. Colliander, Quantifying local lattice distortions in refractory high-entropy alloys, *Phys. Rev. Mater.*, **8**, 083602 (2024).

[103] H. Song, F. Tian and D. Wang, Thermodynamic properties of refractory high entropy alloys, *J. Alloys Compd.*, **682**, 773–777 (2016).

[104] M. Wang, Z. Ma, Z. Xu and X. Cheng, Microstructures and mechanical properties of HfNbTaTiZrW and HfNbTaTiZrMoW refractory high-entropy alloys, *J. Alloys Compd.*, **803**, 778–785 (2019).

[105] O. N. Senkov, D. B. Miracle, K. J. Chaput and J. P. Couzinie, Development and exploration of refractory high entropy alloys - A review, *J. Mater. Res.*, **33**, 3092–3128 (2018).

[106] W. A. Sławiński, Calculation of pair distribution functions for multiphase systems, *J. Appl. Crystallogr.*, **51**, 919–923 (2018).

[107] Y. Hu, S. Guo and M. H. Colliander, Effect of chemical segregation on accuracy of local lattice distortions determination by pair distribution functions, *AIP Adv.*, **14** (2024).

[108] J. Beyer, N. Roth and B. Brummerstedt Iversen, Effects of Voigt diffraction peak profiles on the pair distribution function, *Acta Crystallogr. Sect. A, Found. Adv.*, **78**, 10–20 (2022).

[109] D. Shriver, M. Weller, T. Overton, J. Rourke and F. Armstrong, *Inorganic chemistry*. Oxford University Press, 2018, vol. 7, ISBN: 978–1–4292–9906–0.

[110] E. S. Fisher and C. J. Renken, Single-crystal elastic moduli and the hcp → bcc transformation in Ti, Zr, and Hf, *Phys. Rev.*, **135** (1964).